MOLECULAR MODELING FOR SEPARATION OF XENON

by

Hoa G Nguyen

A dissertation submitted to the faculty of

The University of Utah

in partial fulfillment of the requirements for the degree of

Doctor of Philosophy

Department of Chemistry

The University of Utah

December 2010

The University of Utah Graduate School

STATEMENT OF DISSERTATION APPROVAL

The dissertation of **Hoa G Nguyen**

has been approved by the following supervisory committee members:

Thanh N. Truong	, Chair	**05/05/2010** Date Approved
Edward M. Eyring	, Member	**05/05/2010** Date Approved
Jack Simon	, Member	**05/05/2010** Date Approved
Feng Liu	, Member	**05/05/2010** Date Approved
Scott Anderson	, Member	**05/05/2010** Date Approved

and by **Henry S. White**, Chair of the Department of **Chemistry**

and by Charles A. Wight, Dean of The Graduate School.

ABSTRACT

This dissertation presents a theoretical study on interactions between xenon and transition metals. The focus is on isolated silver and silver clusters doped in chabazite. The ab initio embedded cluster model and *ab initio* periodic calculation were applied for calculations involved the chabazite surface. In the study of xenon binding to small silver clusters on chabazite surface (Chapter 2), the results show that charged clusters have enhanced affinity for xenon. When reduced to neutral, these silver clusters show no xenon affinity. Furthermore, increasing the size of the clusters weakens the xenon adsorption because of the delocalization of the positive charge. In Chapter 3, a comprehensive *ab initio* study on interactions between the transition metal cations of group 10, 11, and 12 and xenon was conducted. The interaction trends of xenon – transition metal cations of group 12 < group 11 < group 10 and row 5 < row 4 < row 6 were found. Pt^+ is found to interact with xenon stronger than Au^+ and is the strongest ligand to Xe ever reported. The nature of the interaction is explained by a σ donation from xenon to the cations. In Chapter 4, the diffusion of xenon inside chabazite structure was studied by the use of the variational canonical transition state theory and the hopping model.

CONTENTS

LIST OF FIGURES

LIST OF TABLES

CHAPTER 1

GENERAL INTRODUCTION

1.1 Theoretical Modeling of Zeolites

Zeolites are microporous crystalline aluminosilicates, composed of edge-sharing SiO_4 and AlO_4 tetrahedra in a framework structure. The silicon and aluminum atoms are called T atoms, and are coordinated with each other through shared oxygen atoms to form unique structures with well-defined pores and channels (Figure 1.1). Except some natural minerals, most widely used zeolites are produced synthetically. Since the discovery of zeolite by Swedish mineralogist Axel Fredrik Cronsted in 1756, many new types of natural zeolites have been explored and a large number of synthetic zeolites have been invented. The main applications of zeolites are adsorbents, separation materials, catalysts and ion exchange materials.[1-4]

A pure silicate structure is charge-neutral. However, the incorporation of a trivalent element changes the properties of the material greatly. The substitution of Al^{3+} for Si^{4+} creates a negative charge which primarily resides at the four oxygen atoms surrounding the aluminum atom. This charge can be balanced by a proton which acts as an acid Brønsted site or by metal cations. These extraframework protons and cations are ion exchangeable and give rise to the rich chemistry of these materials. These active centers can reversibly adsorb polar or polarizable molecules and catalyze chemical reactions. The

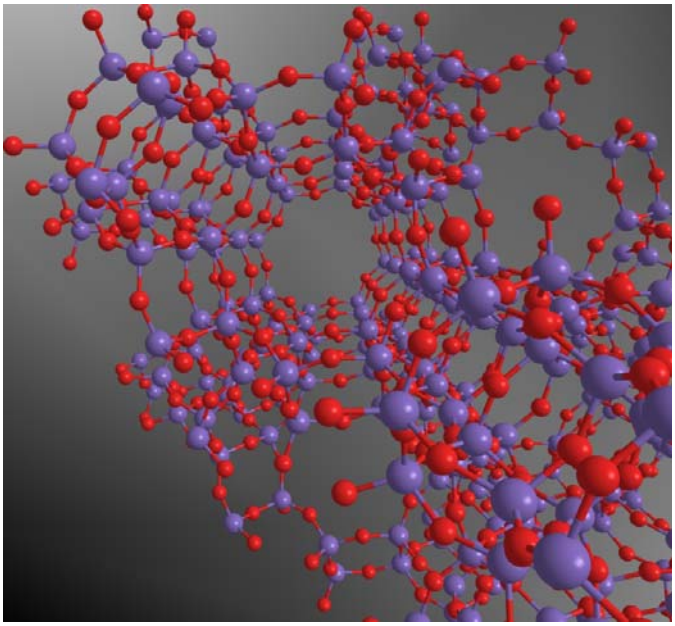

(a)

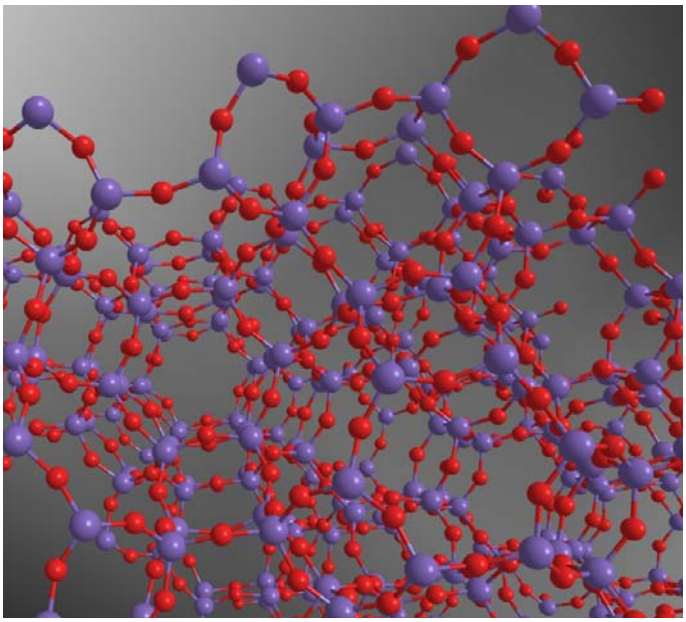

(b)

Figure 1.1 The structural framework of chabazite; 8T (a) and 6T (b) channels.

main theme of this dissertation is to study the interaction between the polarizable xenon atom and these active centers.

Generally, the ratio between silicon and aluminum of one zeolite is important to decide its usage. In catalytic applications, it is desirable to have a more siliceous structure with the extraframework ions residing at well-separated exchanged sites. Zeolites with high silica content are more resistant to high temperatures that occur during the catalytic and regeneration cycles. A high dispersion of acidic protons assures that each proton has the maximum acidic strength. The strong acidity of zeolites promotes hydrocarbon transformation. Zeolites also promote bimolecular reactions, such as intermolecular hydrogen transfer. In more siliceous zeolites, the organophilic nature helps the conversion of polar oxygenated hydrocarbons to paraffins and aromatics. Zeolites are also finding increasing use for synthesis of organic intermediates and fine chemicals. There are many benefits of using zeolites, including options of doping with metals for selective oxidation chemistry, a wide range of possible process operating conditions, waste minimization, easy product separation and catalyst regeneration.

For zeolites used as adsorbents, maximizing the extraframework ion density by raising the number of aluminum atoms increases the extent to which these zeolites are able to hold onto polar adsorbates. Zeolites are used to dry natural and cracking gases, to remove CO_2 from natural gas, to remove pollution like Hg, NO_x, SO_x,. They are also used in other bulk separation applications in petrochemical industry, O_2 from air separation, sugar separation, and amino acids/*n*-nitrosoamines separation. Recently, a very simple adsorbate – the xenon atom – has been studied extensively because of its special binding to zeolitic materials.

Xenon is an extremely rare gas and has long been used in NMR spectroscopy, lasers, illumination, optics, and medicine.[5] There are two new important applications of xenon that can replace traditional but less effective and less environmentally friendly technologies. Firstly, the use of xenon as a fuel for ion thrusters in spaceships could allow the replacement of chemical fuels by nuclear or solar energy in space flight.[6] The second is the use of xenon as an anesthetic due to its clinical and environmental advantages over current anesthetics like N_2O.[7,8] Given the increasing demand, the availability of xenon could become a problem in the future. Because the current way to produce xenon, extracting xenon from air or natural gas in separation plans, is costly, many efforts have been spent on finding an alternative method. The idea of a material that can selectively capture xenon from air is promising since this material can be used in both production and recycle of xenon. Due to their unusual strong binding with xenon, silver-exchanged zeolites are being studied as a candidate for that material.

In the condensed phase science, enormous developments in experimental techniques led to increased resolution of numerous experiments. As a result, detailed information on various zeolite properties is now available. Infrared spectroscopy (IR), Fourier transform infrared spectroscopy (FTIR), and temperature programmed desorption (TPD) can provide fundamental information about the active sites and adsorption modes.[9-11] Insights into catalysts, such as the electronic state, oxidation number or structures, can be obtained by advanced techniques like extended X-ray absorption fine structure (EXAFS), X-ray absorption near-edge structure (XANES), high resolution electron energy loss spectroscopy (HREELS).[12-14] For surfaces of materials, scanning tunneling microscope (STM) and transmission electron microscopy (TEM) can provide

physical pictures at the molecular level.[15,16] Nevertheless, most of the properties and structural parameters of the active sites determined from the experimental means are averaged over the whole structure, making interpretation of experimental data difficult. Another problem of experimental data is the lack of knowledge about the aluminum distribution and about the structural details of extraframework species. The missing information could be achieved by using theoretical tools.

Due to the rapid progress in computers and computational codes, computational approaches to condensed phase problems become more feasible. Nowadays, theoretical calculations not only provide insights into existing systems, but also allow simulation of imaginary species in order to facilitate design of new materials. The most common quantum chemical method for materials is density functional theory (DFT). This is because compared with Hartree-Fock (HF) method or post-HF methods like Møller–Plesset perturbation (MP) theories or coupled-cluster (CC) methods, DFT is less demanding and intrinsically includes electron correlation. Despite these advantages, traditional DFT does not describe well the dispersion interactions, which are often important for zeolite systems, in particular for structure with narrow channels. To overcome this problem, an approach that adds long-range pairwise dispersion corrections to DFT results was suggested.[17]

There are three theoretical models for crystalline microporous materials – the isolated cluster model (gas phase model), the periodic model, and the hybrid embedded cluster model. For some simple cases, the gas phase model is sufficient. This approach treats the interested region of the material quantum mechanically as an isolated system and totally ignores the effects of the remaining crystal framework, namely the steric

hindrance from the pore walls and the electrostatic effect of the lattice. Although using finite clusters to model extended systems is simple and enables the use of very high levels of calculation, it is obviously unrealistic and may lead to incorrect deductions.[2,18-20]

Since the unit cells of zeolites can translates periodically in the three dimensions, the periodic model can be used for zeolitic simulation. Although both the electrostatic effect and the flexibility of the lattice are taken into account, the dominant problem of this model is the demanding computing resources required because the whole frame work is treated equally.[2,18,21] Periodic quantum calculations can be performed with plane wave (PW) basis sets or atomic orbital (AO) basis sets. The main advantage of atomic orbitals is their efficiency. A few tens of localized basis functions per atom are required to represent the Kohn-Sham orbital compared with several hundred functions with the use of PW basis sets. However PW basis sets guarantee wavefunction convergence while AO basis sets do not.

The hybrid embedded cluster models are designed to possess both advantages of the gas phase mode and the periodic model. The most important part of the zeolite structure is modeled with accurate quantum mechanical method and the influence of the rest of the system is modeled with a less expensive methodology. Many embedded cluster model have been proposed so far and have been shown to perform quite well for many studies on adsorption and reaction of zeolites. [2,18,22-24]

This dissertation focused on using the hybrid embedded cluster models to represent the adsorbent effect of zeolites on the xenon atom. Two embedded cluster approaches are discussed. In the first model, called the Surface Charge Representation of the Electrostatic Embedded (SCREEP) model, a finite quantum cluster is embedded in a

potential field generated by two sets of point charges representing the Madelung potential from a periodic structure.[25] In the second model, called the Full Quantum Embedded Cluster (FQEC) model, all lattice effects are included via approximated periodic quantum mechanical calculations while the most interesting part is treated at a more accurate level of calculation. The two methods were tested and compared with each other extensively in previous studies.[26] In this study, they are discussed in more detail in the following sections.

In Chapter 2 and 4, SCREEP and FQEC methods are used to study the interaction between xenon and silver-exchanged chabazite and the diffusion of xenon inside chabazite. In Chapter 3, a comparative study of the interactions between xenon and transition metals of group 10, 11, and 12 is presented. The results of these studies are important for establishing a mechanism of the adsorption of xenon to silver-exchanged zeolites. These understandings will help the designing of new molecular sieves that can capture xenon from the air.

1.2 Embedded Cluster Methodologies

Basically there are two computational methodologies used in zeolite science: (i) molecular mechanics that do not explicitly consider any electron and (ii) quantum mechanics that explicitly take electrons into account. Molecular mechanics can model large compounds quickly whereas quantum mechanics is able to compute many properties and model chemical reactions more accurately. Rigorous quantum mechanics cannot be used for the entire zeolite crystals due to the large size of zeolites. One possible solution of the problem is to limit the quantum mechanical treatment to the active part of

the system, where a high accuracy is required, and to describe the surrounding environment with a less accurate method.

It is possible to combine two methods or more into one calculation, which models a very large compound using molecular mechanics and one crucial section with quantum mechanics. This approach is known as the hybrid quantum mechanics/molecular mechanics (QM/MM) calculations.[2,18,27,28] In the QM/MM approach, the energy of the whole system S is a summation of the energy of the active of the inner part I, the potential function energy of the outer part O, and the interaction between I and O.

$$E_{total}(S) = E_{QM}(I) + E_{pot}(O) + E(I - O)$$

The interaction term is given by the potential function or parts of it, the electrostatic interaction and sometimes the polarization of I by O, described by the QM method.

Complications arise whenever the definition of the QM part requires cutting the bonds that connect the QM part to its environment. Link atoms are needed to terminate the dangling bonds and complete the valency. The energy of the system with link atoms L is given by

$$E_{total}(S) = E_{QM}(C) + E_{pot}(S) - E_{pot}(C) + \Delta$$

where

$$\Delta = -E_{QM}(L) - E_{QM}(L - I) + E_{pot}(L) + E_{pot}(L - I)$$

The term Δ will approach zero if the interatomic potential function mimics the QM potential energy surface for the terminating atoms and their interaction with the inner part

$(L - I)$. With the increasing size of the QM cluster, the interaction between the active site and the link atom region will decrease and the change of Δ will approach zero. It is the change between products and reactants that is important for relative energies, not the absolute values of Δ.

The QM/MM approach is not limited to only the potential field to approximate the environmental effect. It allows the coupling of two quantum mechanical methods when the potential function is replaced by another less expensive quantum calculation.

1.2.1 The Surface Charge Representation of the Electrostatic Embedding Potential (SCREEP) Method

In the linear combination of atomic orbitals-molecular orbitals method (LCAO-MO), one needs analytical expression for matrix elements $\langle \mu | V_{embd}(r) | \upsilon \rangle$ of the embedding potential calculated over basis functions in the cluster. The electrostatic potential from the periodic lattice, or the so-called Madelung potential, makes a dominant contribution to the total embedding potential for many crystals of practical interest. Adding the Madelung potential, $V_{el}(r)$ to the calculation is not a trivial task.

The best known method to accurately calculate the Madelung potential of the periodic system is the Ewald summation method.[29] This can be done by separating the potential energy, a single slowly and conditionally convergent series, into the sum of two rapidly converging series plus a constant term. The total electrostatic interactions is calculated as

$$E_{total} = E^{real} + E^{reciprocal} - E^{correction}$$

where E^{real} is the screened interaction and $E^{reciprocal}$ is due to the canceling Gaussian charge distribution and $E^{correction}$ is the correction term. Although this technique provides an accurate solution for the electrostatic embedding potential, its implementation in existing molecular quantum chemistry programs require significant effort. Alternatively, the Madelung potential could be approximately represented by a finite number of point charges, which are fitted to experimental or any calculation data to provide reasonable results. The reliability of this approach depends on the quality of the point charges.

The surface charge representative of the electrostatic embedding potential (SCREEP) methodology has been proposed for accurately representing the Madelung potential in *ab initio* calculations. This method was based on a theory from electrostatics that no matter what the charge distribution $\rho(r)$ is outside a closed space *C*, its electrostatic potential $V_{el}(r)$ inside *C* can be rigorously replaced by some surface charge density $\sigma_S(r)$ located on the boundary *S* of volume *C*. This could be illustrated as the electrostatic potential inside the conductor independent of the external potential is zero everywhere at equilibrium because free electrons of the conductor respond to the external disturbance by readjusting themselves on the surface to counterbalance the external potential. The conductor boundary conditions are employed as a mathematical device to replace the Ewald summation of matrix elements in quantum calculations. The potential from the charge density $\sigma_S(r)$ exactly compensates the external potential $V_{el}(r)$ for all points *r* on the surface *S* and in its interior.

$$V_{el}(r) + \oint_S \frac{\sigma(r')}{|r - r'|} d^2r' = 0$$

For an imaginary closed surface *S* surrounding the quantum cluster, the electrostatic potential inside surface *S* due to the charge distribution outside the surface can be rigorously replaced with some surface charge density, $\sigma_S(r)$, located on the surface;

$$V_{el}(r) = \oint_S \frac{\sigma_S(r')}{|r - r'|} d^2r'$$

where,

$$\sigma_S(r') = -\sigma(r')$$

Equation 1.6 is exact for all points *r* on the surface *S* and in its interior. Note that the potential generated by $\sigma_S(r)$ outside the surface *S* is generally different from $V_{el}(r)$. The charge distribution $\rho(r)$ may have a so complicated character such as in crystals or in very large molecules that it is not suited for quantum calculations. This approach ensures that the mapping between charge density and charge distribution over a closed surface that provides exactly the same electrostatic potential exists.

For computational reasons the boundary element method is employed to discretize $\sigma_S(r)$ into a set of point charges q_j. In this method, the surface *S* is divided into M surface elements with areas S_j and the surface charge density is now represented by a set of M point charges q_j located at the centers of surface elements r_j;

$$q_j = \sigma_S(r_j) \times S_j$$

This approximation is accurate when the numbers of surface points M is large enough and the surface *S* and the charge distribution are sufficiently smooth. Then equation 1.6 can be approximated in a matrix form as

$$\boldsymbol{V} - \boldsymbol{A}\boldsymbol{q} = \boldsymbol{0}$$

The column vector surface charges $\boldsymbol{q}$ can be determined by solving systems of linear equations. The vector $\boldsymbol{V}$ contains the values of the external electrostatic potential at point $r_j\big(V_j = V_{el}(r_j)\big)$. $\boldsymbol{A}$ is the $M \times M$ nonsingular square matrix with elements

$$A_{ij} = \frac{1}{|r_j - r_i|} \text{ for } i \neq j \text{ and } A_{ij} = 1.07\sqrt{\frac{4\pi}{S_j}}$$

Nondiagonal elements A_{ij} represent a generic Coulombic interaction between the surface elements r_i and r_j. $|r_j - r_i|$ is the distance between a point charge located at r_j on the surface *S* and a position r_i where the potential is calculated.

In this approach, the Madelung potential V_j is calculated using the Ewald summation technique. The matrix inversion algorithm has been used to solve for $\boldsymbol{q}$. The calculation of $\boldsymbol{q}$ proceeds in three steps: (1) Construct and discretize the SCREEP surface around a quantum cluster, (2) Calculate the Madelung potential V_j on the surface elements by the Ewald summation technique, and (3) solve the linear equation 1.9 for $\boldsymbol{q}$. $\boldsymbol{q}$ should be determined once prior to their use in embedded cluster calculations.

In the SCREEP embedded model, the model is composed of three layers. At the center of the model is a quantum mechanical cluster taken from the crystal structure to represent the most important part of the system of interest. The other two layers (i.e. the

explicit charges and the surface charges) in this model are to describe the Madelung potential of the extended framework. The explicit charges are a set of partial atomic charges located at the zeolites atomic sites. This layer attempts to represent the local electrostatic interactions around the site of interest. Due to the poor convergence of the Madelung potential, the explicit point charges alone are not able to accurately reproduce the electrostatic potential of the periodic framework. The surface charges, determined by the SCREEP method, are added as the third layer to represent the remainder of the Madelung potential.

The lattice charges used to determine $V_{el}(r)$ as the reference potential can be derived from a Muliken population analysis of a periodic calculation. However, those determined from periodic HF with 3-21G basis set are very close to half of their formal charges. Half of the formal charge is used in this study. The lattice charges close the quantum clusters are treated explicitly and thus the electrostatic potential resulted from these charges is exact. The electrostatic potential from the rest of the lattice point charges, not included as explicit charges, is recovered by the potential from the surface charge. This separation can dramatically decrease the error resulting from discretizing the surface charge density to the point charges on the surface. The surface charges have been created in such a way that they cover all the quantum cluster and the proximity where the chemistry occurs. The shape of the surface *S* is arbitrary and should have no effect to the final result.

1.2.2 Full Quantum Embedded Cluster (FQEC) Model

The central idea of the embedded cluster methodology is to divide the physical system into two regions, the active and the spectator regions. In the full quantum

embedded cluster approach, not only the active region but also the spectator region is treated quantum mechanically.[30] For periodic systems, like zeolite, the spectator region is treated by a periodic electronic structure theory. The partition of the physical system within the periodic boundary condition is illustrated in Figure 1.2.

The total energy of the system can be expressed within the framework of the IMOMO methodology developed by Morokuma and co-workers[31] as

$$E_{total} = E_{crystal}^{low} + \left(E_{cluster}^{high} - E_{cluster}^{low}\right) + \Delta E_{boundary}$$

In the first term, interactions in all regions, the active and the spectator regions of the crystal and the cross-term interactions between the two regions, are represented within a low level of periodic quantum mechanical formalism. The second term, $\left(E_{cluster}^{high} - E_{cluster}^{low}\right)$, represents the correction to the local interactions in the active region a more accurate level of electronic structure theory. The last term, $\Delta E_{boundary}$, represents the difference in energy of the boundary region calculated at the two levels of

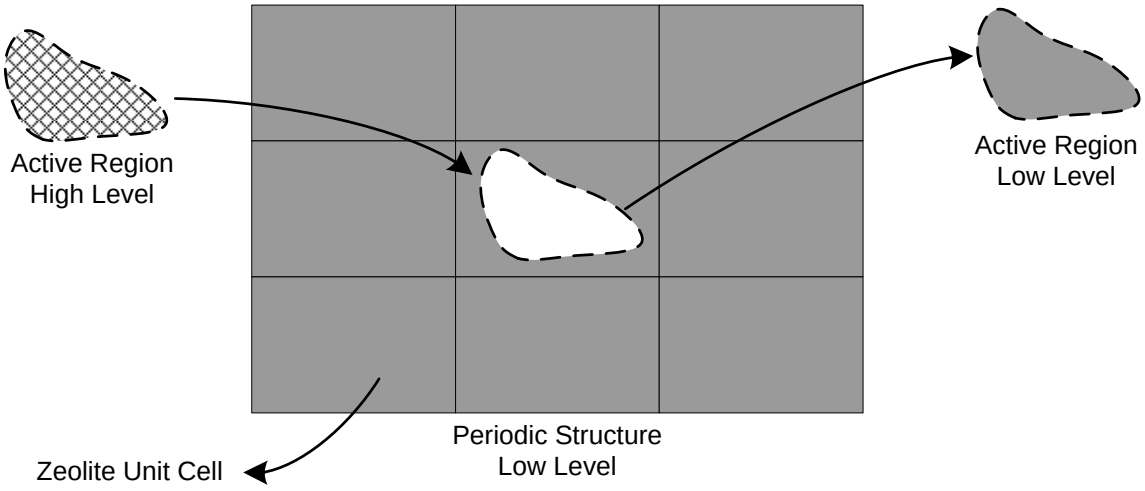

Figure 1.2 Schematic description of the FQEC methodology

theory. With a careful choice of the boundary region, the last term can be made to remain nearly constant in a chemical process and thus has no effect on the relative energy; consequently it can be ignored.

Correction for the local interactions in the active region can be done at any level of quantum chemistry methods available for isolated systems. Since the interactions in the most important region can be corrected, it is possible to use a less accurate periodic electronic structure method to model interactions in the crystal. For $E_{crystal}^{low}$, we propose to use the SIESTA program (Spanish Initiative for Electronic Simulations with Thousands of Atoms) developed by Soler et al.[32]

The SIESTA program is a self-consistent density functional theory method using standard norm-conserving pseudopotentials and flexible, numerical linear combination of atomic orbital basis sets. SIESTA uses localized Wannier-like electron wavefunctions which allow sparsity of the Hamiltonian and overlap matrices to facilitate calculations that scale linearly with the size of the system. This method allows very fast simulations with minimal basis sets and accurate calculations with complete multiple-zeta and polarized bases, depending on the required accuracy and available computing power.

1.3 References

(1) *Handbook of Zeolite Science and Technology*; Auerbach, S. M.; Carrado, K. A.; Dutta, P. K., Eds.; Marcel Dekker, Inc., 2003.

(2) Cejka, J.; Bekkum, H. v.; Corma, A.; Schüth, F. *Introduction to Zeolite Science and Practice*; Elsevier, 2007.

(3) Garlarneau, A.; Renzo, F. D.; Fajula, F.; Vedrine, J. *Zeolites and Mesoporous Materials at The Dawn of The 21st Century*; Elsevier, 2001.

(4) *Zeolite Chemistry and Catalysis*; Rabo, J. A., Ed.; American Chemical Society, 1976.

(5) Häussinger, P.; Glatthaar, R.; Rhode, W.; Kick, H.; Benkmann, C.; Weber, J. In *Ullmann's Encyclopedia of Industrial Chemistry*; Wiley: 2001.

(6) Zona, K. *Innovative Engines: Glenn Ion Propulsion Research Tames the Challenges of 21st century Space Travel*, 2006.

(7) Goto, T. *Canadian Journal of Anesthesia / Journal canadien d'anesthésie* **2002**, *49*, 335.

(8) Tonner, P. H. *Current Opinion in Anesthesiology* **2006**, *19*, 382.

(9) Henderson, M. A. *Surface Science* **1996**, *355*, 151.

(10) Kuroda, Y.; Yoshikawa, Y.; Kumashiro, R.; Nagao, M. *Journal of Physical Chemistry B* **1997**, *101*, 6497.

(11) Grunwaldt, J. D.; Baiker, A. *Journal of Physical Chemistry B* **1999**, *103*, 1002.

(12) Samant, M. G.; Boudart, M. *Journal of Physical Chemistry* **1991**, *95*, 4070.

(13) Mojet, B. L.; Miller, J. T.; Ramaker, D. E.; Koningsberger, D. C. *Journal of Catalysis* **1999**, *186*, 373.

(14) Lamberti, C.; Bordiga, S.; Zecchina, A.; Salvalaggio, J.; Geobaldo, F.; Otero, A. *Journal of Chemical Society, Faraday Transaction* **1998**, *94*, 1519.

(15) Fischer, S.; Munz, A.; Schierbaum, K. D.; Goepel, W. *Surface Science* **1995**, *337*, 17.

(16) Kazuo, F. *Science and Technology of Advanced Materials* **2008**, *9*, 014110.

(17) Grimme, S. *Journal of Computational Chemistry* **2006**, *27*, 1787.

(18) *Ordered Porous Solid*; Valtchev, V.; Mintova, S.; Tspatsis, M., Eds.; Elsevier, 2009.

(19) Sauer, J. *Studies of Surface Science and Catalysis* **1994**, *84*, 2039.

(20) Brand, H. V.; Curtiss, L. A.; Iton, L. E. *Journal of Physical Chemistry* **1993**, *97*, 12773.

(21) Catlow, C. R. A. *Modeling of Structure and Reactivity in Zeolites*; Academic Press: San Diego, 1992.

(22) Clementi, E. *Lecture Notes in Chemistry, Vol 19: Computational Aspects for Large Chemical Systems* **1980**.

(23) Gao, J.; Amara, P.; Alhambra, C.; Field, M. J. *Journal of Physical Chemistry A* **1998**, *102*, 4714.

(24) Hillier, I. H. *THEOCHEM* **1999**, *45*, 463.

(25) Stefanovich, E. V.; Truong, T. N. *Journal of Physical Chemistry B* **1998**, *102*, 3018.

(26) Treesukol, P.; Lewis, J. P.; Limtrakul, J.; Truong, T. N. *Chemical Physics Letters* **2001**, *350*, 128.

(27) Sierka, M.; Sauer, J. *Faraday Discussion* **1997**, *106*, 41.

(28) Sherwood, P. In *Modern Methods and Algorithms of Quantum Chemistry*; Grotendorst, J., Ed.; John von Neumann Institute for Computing: 2000.

(29) Ewald, P. *Annalen der Physik* **1921**, *64*, 253.

(30) Treesukol, P.; Lewis, J. P.; Limtrakul, J.; Truong, T. N. *Chemical Physic Letters* **2001**, *350*, 128.

(31) Svensson, M.; Humbel, S.; Morokuma, K. *Journal of Chemical Physics* **1996**, *105*, 1959.

(32) Soler, J. M.; Artacho, E.; Gale, J. D.; Garcia, A.; Junquera, J.; Ordejon, P.; Sanchez-Portal, D. *Journal of Physics: Condensed Matter* **2002**, *14*, 2745.

CHAPTER 2

THEORETICAL STUDY ON THE INTERACTION BETWEEN XENON AND POSITIVE CHARGED SILVER CLUSTERS

2.1 Introduction

Although rare and expensive, xenon has a number of important applications in lighting, lasers and the medical industry. In medicine, xenon is a promising general anesthetic[1] while in the aerospace industry, it is a preferred fuel for the ion thruster in spacecrafts. Xenon has also been used as a research tool for ^{129}Xe NMR studies of zeolite structures and activity, particularly the location of acidic sites.[2] An excellent review on xenon's properties, application and production can be found in the work of Häussinger et al.[3] Currently, xenon is produced by a costly process of fractional distillation of liquefied air. Given the increase in demand, alternative methods for producing xenon are of great interest. One recent study demonstrated the use of a polymer membrane to separate xenon from oxygen and nitrogen.[4]

Zeolites, particularly silver-exchanged zeolites, are also being studied as promising materials for xenon separation. Xe was found to exhibit unusually strong interactions with silver-exchanged zeolites.[5-13] Furthermore, it has been shown that Xe is adsorbed more strongly in the silver-exchanged X and Y zeolites than in their sodium counterparts.[5-8] In Y zeolite, the initial isosteric heats of adsorption of xenon on Ag-exchanged and Na-exchanged materials were 31.0 kJ/mol and 18.5 kJ/mol, respectively.[10] Recently, experimental studies conducted by Munataka et al.,[11] Kuznicki

et al.[12] and us[13] have also shown that xenon can bind strongly to Ag-exchanged mordenite, Ag-exchanged ETS-10 (a type of titanosilicate) and Ag-exchanged chabazite, respectively. Although silver is necessary for zeolites to bind xenon, the nature of this unusually strong binding is still controversial.

Ionic silver was often thought to be the binding site for xenon based on the observed trend in the strength of the interaction of xenon with oxidized > untreated > reduced AgX zeolites.[6] Both reduced AgX and untreated NaX are inert to xenon adsorption. Similarly, in our unpublished experimental study,[13] silver exchanged chabazite also loses its affinity for xenon after reduction. However, in the study on Ag-ETS-10, Kuznicki et al. concluded the strong binding with xenon is a result of its interaction with silver nanoparticles due to the lack of the yellow coloration generally associated with Ag^+ ions in molecular sieves.[12] This raises the question as to the nature of the binding site of Xe in Ag-exchanged zeolites, namely silver exchanged ion sites inside zeolite or silver nano-clusters on the zeolite surface as shown in Figure 2.1.

From the electronic configuration of Ag^+, $(4d)^{10}(5s)^0$, it was suggested that the large heat of adsorption of Xe on AgX and AgY zeolites is due to the d_π-d_π back-donation from Ag^+ to Xe.[5-7] The d_π-d_π back-donation involves electron donation from the 4d orbital of Ag^+ to the virtual 5d orbital of Xe. Such back-donation was also thought to be responsible for the unusual negative chemical shifts observed in the ^{129}Xe NMR in AgX and AgY zeolites.[6,7] It is interesting to note that the d_π-d_π back-donation indicates a charge transfer from the silver cation to xenon. However, a theoretical study by Freitag et al.[14] found that charge is transferred from Xe to Ag^+ with no indication of a 4d to 5d donation from Ag^+ to Xe. Furthermore, the experimental and theoretical works on AgA

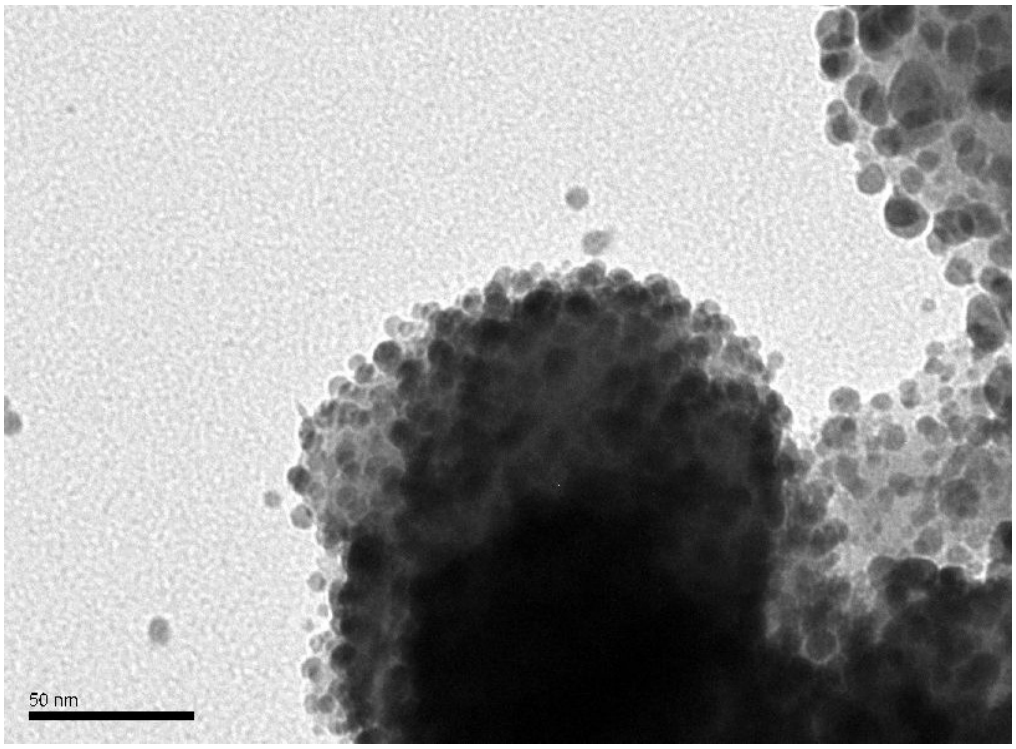

Figure 2.1 Transmission electron microscope (TEM) image of silver exchanged chabazite from our unpublished experimental work.[13] Scale bar is 50 nm.

zeolite of Moudrakovski et al.[15] and Jameson et al.[16] found only positive chemical shifts. They argued that this is because Xe atoms are physisorbed in AgA zeolite rather than chemisorbed as in the work of Freitag et al. In their view, the negative chemical shifts in AgX and AgY zeolites remain a puzzle.

In the present work, we carried out a systematic theoretical study on the interaction of xenon with Ag^+ and small silver clusters in both the gas-phase and adsorbed on chabazite surface. From our preliminary experimental data[13] and that of Kuznicki et al.,[17] the adsorption of xenon occurs on the surface of zeolite with ionic or metal silver nanoparticles serving as possible binding sites (Figure 2.1). The objective of this study was to provide a fundamental understanding of the nature of the interaction between Xe and Ag clusters on zeolite by determining: (1) the structural and electronic properties of the silver nanoparticles on the chabazite surface and (2) how these properties govern the

affinity of Xe. Quantum chemistry calculations were performed using cluster models to represent the binding site. The size of the Ag_n clusters was limited to four atoms in this study. The NBO population analyses[18] were used to study the electronic structures of the silver clusters. This method was previously used by Chen and Yang[19] to discover the d-π^* back-donation between Ag-exchanged zeolite and O_2, N_2 and ethylene. In addition, we studied the interaction between Xe and a Na-exchanged chabazite system for comparison purposes.

2.2 Computational Details

For calculations involving free silver clusters in the gas phase, the optimized cluster structures from previous studies[20,21] were used as the starting points. For Xe–Ag-chabazite systems, cluster models were used to represent the binding sites of the zeolite materials. A cluster model of the zeolite binding site was made by cutting selected atoms surrounding the binding site from the crystal structure of chabazite taken from the Database of Zeolite Structures.[22] In the cluster model, the zeolite and Xe are treated quantum mechanically. More discussion on the accuracy of the cluster model and its application to zeolite systems can be found elsewhere.[23]

In the chabazite cage, the preferred site of Ag^+ is on top of the 6T ring.[24,25] Because Ag^+ is the seed for growing Ag clusters on zeolite, we assumed the binding site for silver clusters is on the top of the 6T ring. The (001) surface was chosen for modeling because it is the only surface on which these 6T rings are fully exposed. Figure 2.2 shows three types of 6T rings on the (001) surface denoted R1, R2 and R3. In Figure 2.2.e, calculated results indicated that a seed Ag^+ ion placed on R2 would sink deep inside the zeolite framework and R2 would shield the adsorbed Ag^+ from binding to additional silver

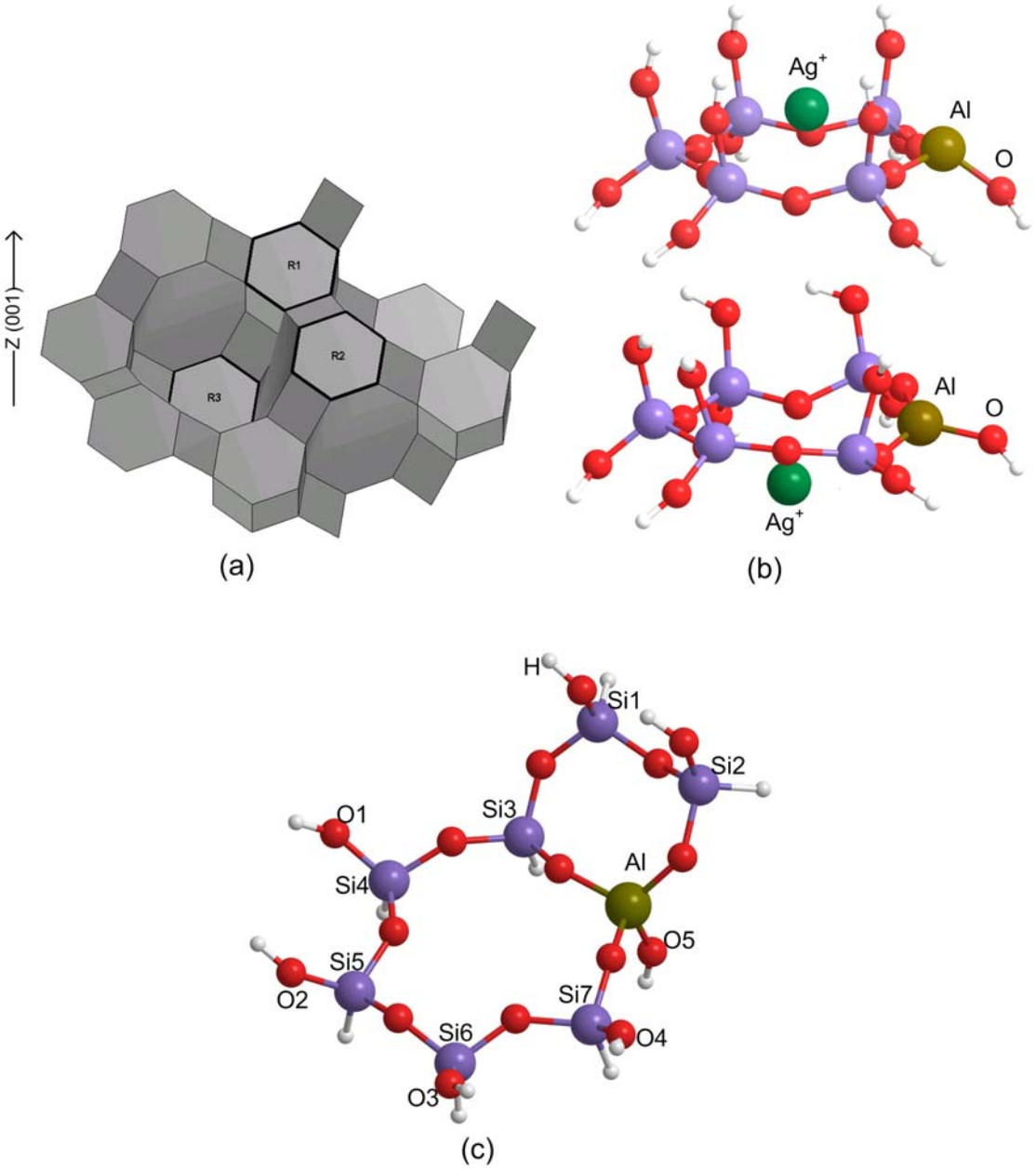

Figure 2.2 Chabazite (001) surface. (a) Three types of 6T ring R1, R2 and R3 on the (001) surface of chabazite structure. (b) Starting (top) and ending geometry of the system of a silver atom placed on top of an R2 ring (c) $[Si_7AlO_{16}H_{14}]$ cluster created by cutting the R1 site out of the chabazite surface.

atoms, thus preventing clusters formation on R2. For the R1 site, the adsorbed Ag^+ is exposed above the surface and would be a good seed for other silver atoms to bind. The R3 site is similar to R1, however, the 4T and 8T rings surrounding it might hinder the agglomeration of silver atoms. For these reasons, we have selected the R1 site for this study. At the R1 site, one tetrahedral site is selected to be the Brönsted acidic site and is substituted by one aluminum atom. To avoid edge effects in the cluster model, the 4T ring at the corner of the Al binding site is added (see Figures 2.2.b and 2.2.c). On the chabazite surface (Figure 2.2.a), Si atoms in the R1 sites are saturated while Si atoms in the R2 sites are not. Therefore, the Si atoms in R2 are capped with OH groups, which is how Si1 and Si2 in Figure 2.2.c were treated. These OH groups were not constrained during optimization. The cluster model of the binding site contained unsaturated O and Si atoms as the result of cutting the cluster model out of the chabazite crystal structure. These atoms (Si1-7 and O1-5 in Figure 2.2.c) were capped by H atoms which were kept fixed during optimization while atoms in the 6- and 4-member rings and the oxygen atoms of OH groups at Si1 and Si2 were allowed to move. The final $[Si_7AlO_{16}H_{14}]$ quantum cluster represents the best compromise between adequate structural representation of chabazite for studying adsorption of metal clusters and computational demand for a reasonable number of quantum chemistry calculations. In the discussion below, [Cha] is used to denote $[Si_7AlO_{16}H_{14}]$ with Ag^+[Cha] denoting one silver cation on the R1 site of the (001) surface.

Second-order Møller–Plesset (MP2) perturbation theory calculations and nonlocal hybrid B3LYP density functional theory (DFT) were used in this study. The DFT/B3LYP level of computation is well-known for its consistency and reliability for studying interaction in zeolites. Since the focus of this study is on $Xe–Ag_n^+$ systems rather on

neutral systems, the B3LYP method would be reasonably accurate despite some known inadequacies in describing dispersion interactions.[26,27] The 6-31G(d, p) basis set was used for the aluminum, silicon, hydrogen and oxygen atoms in the 6T and 4T rings, and the LANL2DZ basis set with the effective core potential was used for the silver atom. Xenon was treated with the 3-21G(d) basis set. These basis sets of silver and xenon are sufficient since they yield a potential curve in agreement with those from the recent more accurate *ab initio* study of Yousef et al.[28] on smaller systems. To study the excited states of the $Xe–Ag^+$, we employed the complete active space self-consistent field (CASSCF (2,4)) with the all electron relativistic basis set of Koga et al.[29,30] The counterpoise (CP) method[31,32] was applied to correct the basis set superposition error in the binding energies.

The cluster model ignores the effects of the extended zeolite framework on the adsorption properties mostly due to the Madelung potential from crystal atoms outside the cluster. A previous study on the adsorption of NO and CO on Cu-ZSM-5[33] found that such effects are small. One would also expect these effects to be small in Xe on Ag_n^+[Cha] system. To confirm this, we have performed embedded cluster calculations for the $Xe–Ag^+$[Cha] system. To incorporate the environmental effects of the framework, we embedded the quantum cluster in a potential field of point charges. The Surface Charge Representation of the Electrostatic Embedded Potential (SCREEP) method[34] was used to construct these point charges. This methodology has been successfully employed in a number of zeolite systems.[33,35-38] B3LYP calculations for adsorption of Xe on the Ag_n^+ showed no major difference in the results from the cluster and embedded cluster models. Specifically, the calculated binding energies of Xe to Ag^+ on the chabazite surface under embedded cluster and cluster model are 37.4 and 37.1 kJ/mol, respectively.

Consequently, for simplicity we employed only the cluster model to model the chabazite binding site in this study. All calculations were done using the Gaussian03 program.[39]

2.3 Results

2.3.1 Gas Phase

2.3.1.1 Xe–Ag^+

Studies on the binding between isolated monoatomic Ag^+ and xenon can provide a reference point for studying the adsorption of Xe on the Ag_n^+[Cha] systems. The most accurate calculation to date for the Xe–Ag^+ potential curve was done by Yousef et al.[28] using the CCSD(T) level of theory with the quintuple-ζ basis set. The predicted binding energy of 70.06 kJ/mol is consistent with the established experimental lower limit of 47 kJ/mol.[40] The potential energy curves for Xe–Ag^+ from previous studies and our calculations are shown in Figure 2.3. Note that the present B3LYP calculations with the LANL basis set for Ag^+ yield D_e=73.91 kJ/mol and R_e=2.87 Å. This agrees well with D_e=70.06 kJ/mol and R_e=2.76 Å from CCSD(T) results from Yousef et al. The calculated MP2 binding energy of 50.63 kJ/mol is somewhat smaller but is still consistent with the established experimental lower limit of 47 kJ/mol. This result supports the choice of the B3LYP functional and the basis set used in this study.

NBO analysis can provide insight into the nature of the donor-acceptor interaction in the Xe–Ag^+ system. The electron occupancies of the important atomic orbitals, namely the 5s, 4d, and 5p orbitals of Ag^+ and the 5p and 5d orbitals of Xe before and after adsorption are listed in Table 2.1. Upon adsorption 0.14 electron is transferred from Xe's 5p to Ag^+ virtual 5s orbital. This is referred to as the σ donation due to the nature of the binding orbital of Xe–Ag^+.

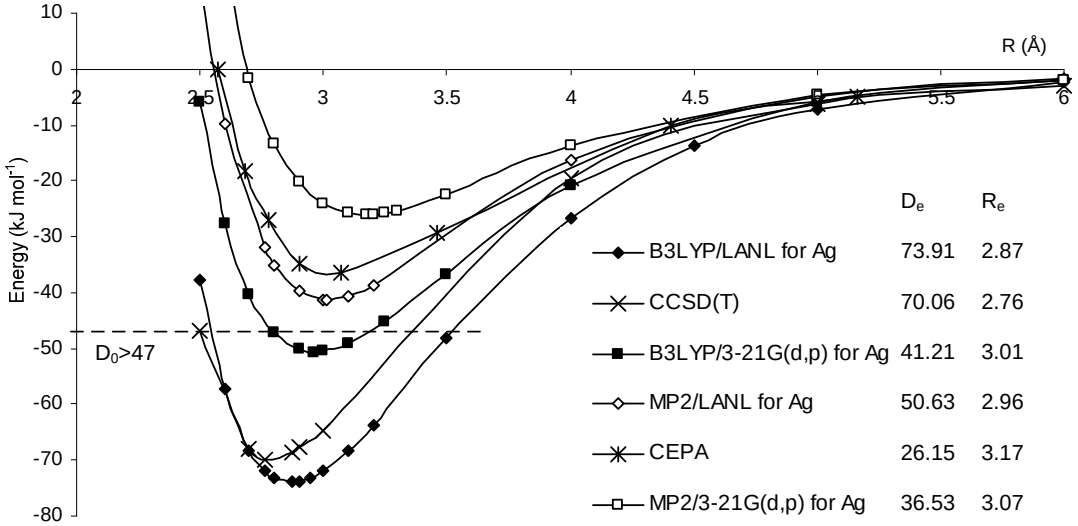

Figure 2.3 Potential energy curves for gas phase Xe–Ag^+ compound. D_e and R_e are the potential depth and equilibrium distance, respectively.

Table 2.1 B3LYP/LANL NAO (Natural Atomic Orbital) Electron Occupancies of Gas Phase Ag^+ and Xe Before and After Binding

$Ag^+ + Xe$	Ag^+_{before}	$(5s)^{0.0000}$	$(4d)^{10.0000}$	$(5p)^{0.0000}$
	Ag^+_{after}	$(5s)^{0.1373}$	$(4d)^{9.9920}$	$(5p)^{0.0115}$
	$\mathbf{Ag^+_{\Delta}}$ [a]	$\mathbf{(5s)^{0.1373}}$	$\mathbf{(4d)^{-0.0080}}$	$\mathbf{(5p)^{0.0115}}$
	Xe_{before} [b]	$(5p)^{6.0000}$	$(5d)^{0.0000}$	
	Xe_{after} [b]	$(5p)^{5.8535}$	$(5d)^{0.0065}$	
	$\mathbf{Xe_{\Delta}}$ [a]	$\mathbf{(5p)^{-0.1465}}$	$\mathbf{(5d)^{0.0065}}$	
$Na^+ + Xe$	Na^+_{before}	$(3s)^{0.0000}$	$(3p)^{0.0000}$	
	Na^+_{after}	$(3s)^{0.0279}$	$(3p)^{0.0075}$	
	$\mathbf{Na^+_{\Delta}}$	$\mathbf{(3s)^{0.0279}}$	$\mathbf{(3p)^{0.0075}}$	
	$\mathbf{Xe_{\Delta}}$	$\mathbf{(5p)^{-0.0414}}$	$\mathbf{(5d)^{0.0040}}$	

[a] $_{\Delta}$ indicates the differences in electron occupancies between before and after binding.

[b] The electronic configurations of Xe before binding is always $(5p)^{6.0000}(5d)^{0.0000}$. Therefore Xe_{before} and Xe_{after} will be omitted in the following tables.

The d_π-d_π back-donation suggested by Gedeon et al.[6] as a crucial factor for the Xe–Ag^+ interaction was not confirmed in this study. In Table 2.1, only 0.0080 electron charge transfers out of the Ag^+'s 4d and 0.0065 electron is received by the Xe's 5d orbitals. This indicates the magnitude of the d_π-d_π back-donation is insignificant. Compared to the σ donation, it is smaller by a factor of 1:18. We note that the magnitude of the d_π-d_π back-donation was found to be slightly larger for adsorption of N_2, O_2 or ethylene on Ag^+ in zeolite by Chen and Yang[19] but is also much smaller compared to the σ donation found here for the Xe–Ag^+[Cha] system. The present results indicate that the σ donation is the dominant factor governing the interaction of Xe with the Ag^+ cation in the ground state whereas the d_π-d_π back-donation plays an insignificant role. This differs from previous suggestions on the role of the d_π-d_π back-donation for this system.[5-7]

Since the Ag^+ cation has several low lying excited states, it is possible that the d_π-d_π back-donation is more noticeable in the excited state of Xe–Ag^+. To investigate such a possibility, CASSCF(2,4) calculations were carried out for several low-lying electronic states of Xe-Ag^+. In particular, these include the ^1S ground state corresponding to the electronic configuration $(4d)^{10}$ of Ag^+, and the first and second excited states, ^3D and ^1D, respectively corresponding to the Ag^+ configuration $(4d)^9(5s)^1$.

Figure 2.4 shows the potential energy curves for the three lowest electronic states of Xe–Ag^+. For Ag^+, CASSCF calculations yield the first and second excitation energies of 461.6 and 506.1 kJ/mol as compared to the experimental data of 467.8 and 550.4 kJ/mol.[41] The electronic configurations are listed in Table 2.2. Compared with the B3LYP results, the CASSCF calculations predict smaller magnitudes of both the σ donation and the d_π-d_π back-donation for the ground state. The difference between the excited states and the ground state is the promotion of one electron from 4d to 5s in Ag^+.

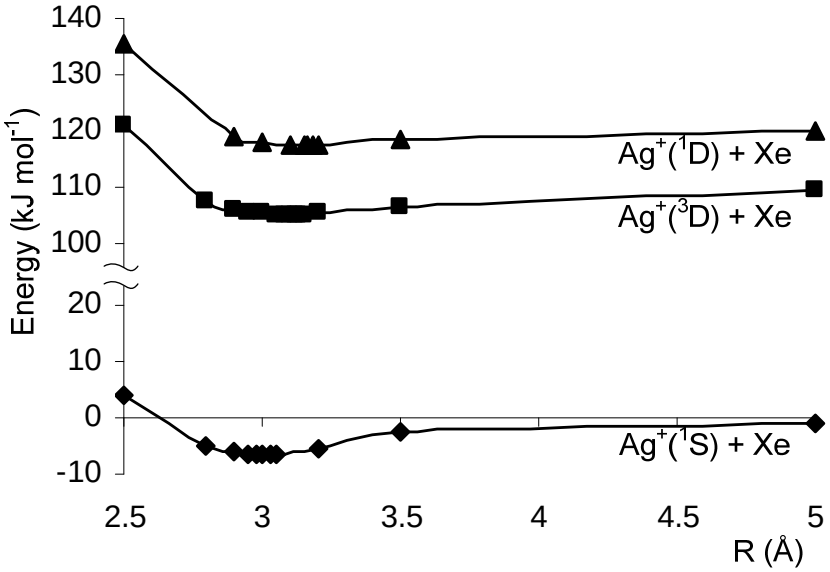

Figure 2.4 CASSCF potential energy curves for the ground state and the first two excited states of Xe–Ag^+ compound.

Table 2.2 CASSCF NAO Electron Occupancies of Gas Phase Ag^+ and Xe Before and After Binding

$Ag^+(^1S)$ + Xe	Ag^+_{before}	$(5s)^{0.0000}$	$(4d)^{10.0000}$	$(5p)^{0.0000}$
	Ag^+_{after}	$(5s)^{0.0341}$	$(4d)^{9.9973}$	$(5p)^{0.0073}$
	Ag^+_{Δ}	**$(5s)^{0.0341}$**	**$(4d)^{-0.0027}$**	**$(5p)^{0.0073}$**
	Xe_{Δ}	**$(5p)^{-0.0578}$**	**$(5d)^{0.0145}$**	
$Ag^+(^3D)$ + Xe	Ag^+_{before}	$(5s)^{1.0000}$	$(4d)^{9.0000}$	$(5p)^{0.0000}$
	Ag^+_{after}	$(5s)^{1.0256}$	$(4d)^{9.0304}$	$(5p)^{0.0181}$
	Ag^+_{Δ}	**$(5s)^{0.0256}$**	**$(4d)^{0.0304}$**	**$(5p)^{0.0181}$**
	Xe_{Δ}	**$(5p)^{-0.0888}$**	**$(5d)^{0.0096}$**	
$Ag^+(^1D)$ + Xe	Ag^+_{before}	$(5s)^{1.0000}$	$(4d)^{9.0000}$	$(5p)^{0.0000}$
	Ag^+_{after}	$(5s)^{1.0198}$	$(4d)^{9.0271}$	$(5p)^{0.0171}$
	Ag^+_{Δ}	**$(5s)^{0.0198}$**	**$(4d)^{0.0271}$**	**$(5p)^{0.0171}$**
	Xe_{Δ}	**$(5p)^{-0.0798}$**	**$(5d)^{0.0090}$**	

This reduces the amount of electron transfer to Ag^+'s 5s in the excited states. The charge transfers to the Ag^+'s 5s for the ground state, first and second excited states are 0.0341, 0.0256 and 0.0198 electron, respectively. In the excited states, because Ag^+'s 4d orbital has only 9 electrons, this orbital can receive electron from Xe's 5p upon binding. The occupancy change in Ag's 4d is -0.0027, 0.0304, and 0.0271 electron for the ground state, ^3D and ^1D excited states, respectively. For the d_π-d_π back-donation, the 4d orbital of silver is the electron acceptor, thus there is no d_π-d_π back-donation in the excited states of the Xe–Ag^+ system.

2.3.1.2 Xe–Na^+

For comparison, the binding energy between Xe and Na+ was also calculated and has the magnitude of 46.08 kJ/mol (Table 2.3) as compared to 73.91 kJ/mol for Xe–Ag+. The charge transferred to Na+'s 3s from Xe's 5p is 0.028 electron as compared to 0.14 electron in the Xe–Ag^+ system. It is known that the degree of electron transfer is proportional to the overlap between the donor and acceptor orbitals. Since Na^+'s 3s orbital is much smaller than the Ag^+'s 5s orbital, which is comparable in size to Xe's 5p orbital, one can expect smaller overlap between the Na^+'s 3s orbital and Xe's 5p orbital and thus a smaller amount of charge transfer. These results further support the importance of the σ donation.

2.3.1.3 Xe–Ag2,3,4+

The optimized structures of Xe adsorbed on Ag2,3,4+ clusters are shown in Figure 2.5. The binding energies between xenon and the silver cation clusters are given in Table 2.3. The electronic configuration of the silver atom that binds directly to xenon indicated

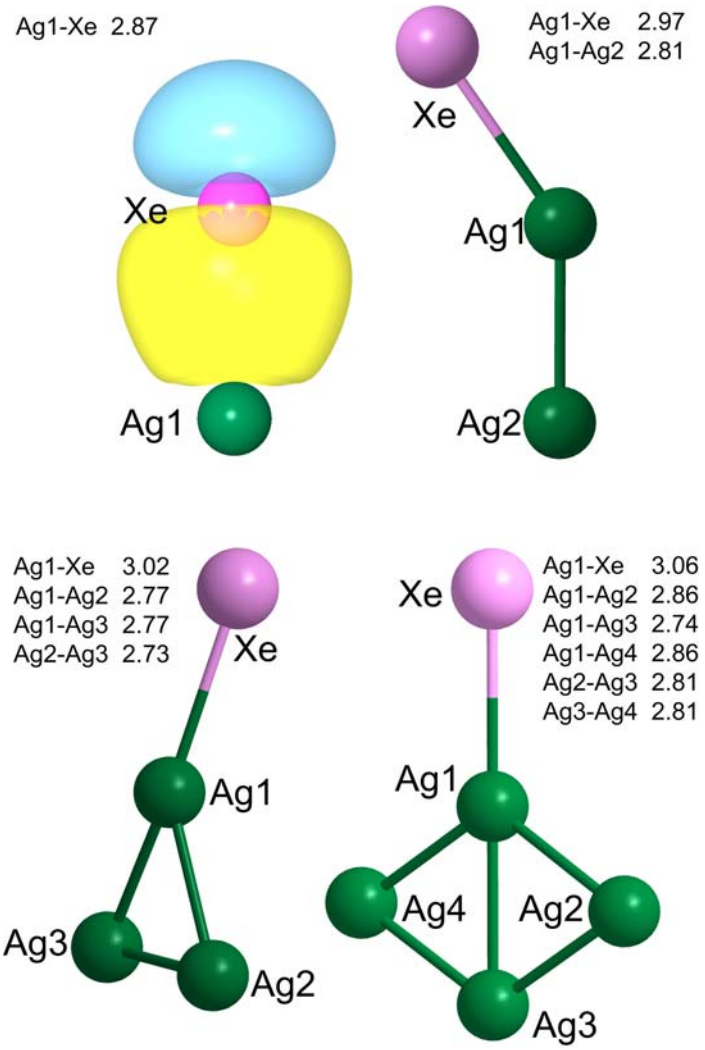

Figure 2.5 Xenon binds to gas phase Ag_n^+ clusters. σ donation bonding orbital of Xe and Ag^+ is generated using NBOView.[18] Distances (Å) between silver and xenon atoms are shown.

Table 2.3 Binding Energy D_e (kJ/mol) and Equilibrium Distance R_e (Å) of Xe and Gas Phase Neutral, Positive Ag Clusters and Na^+ Cation

B3LYP/LANL for Ag, with CP correction		
	D_e	R_e
Ag_1^+	73.91	2.87
Ag_2^+	42.64	2.97
Ag_3^+	33.29	3.02
Ag_4^+	27.62	3.06
Na^+	46.08	3.04

Table 2.4 B3LYP/LANL NAO Electron Occupancies of Gas Phase $Ag_{2,3,4}^{+}$ cluster and Xe Before and After Binding

Ag_2^{+}+Xe	$Ag1_{before}$	$(5s)^{0.4983}$	$(4d)^{9.9851}$	$(5p)^{0.0165}$
	$Ag1_{after}$	$(5s)^{0.5593}$	$(4d)^{9.9816}$	$(5p)^{0.0169}$
	$Ag1_{\Delta}$	**$(5s)^{0.0536}$**	**$(4d)^{-0.0034}$**	**$(5p)^{0.0004}$**
	$Ag_2^{+}{}_{before}$	$(5s)^{0.9967}$	$(4d)^{19.9701}$	$(5p)^{0.0329}$
	$Ag_2^{+}{}_{after}$	$(5s)^{1.1113}$	$(4d)^{19.9639}$	$(5p)^{0.0456}$
	$Ag_2^{+}{}_{\Delta}$	**$(5s)^{0.1146}$**	**$(4d)^{-0.0063}$**	**$(5p)^{0.0127}$**
	Xe_{Δ}	**$(5p)^{-0.1167}$**	$(4d)^{9.9773}$	**$(5d)^{0.0034}$**
Ag_3^{+}+Xe	$Ag1_{before}$	$(5s)^{0.6689}$		$(5p)^{0.0201}$
	$Ag1_{after}$	$(5s)^{0.7190}$	$(4d)^{9.9697}$	$(5p)^{0.0281}$
	$Ag1_{\Delta}$	**$(5s)^{0.0501}$**	**$(4d)^{-0.0077}$**	**$(5p)^{0.0080}$**
	$Ag_3^{+}{}_{before}$	$(5s)^{2.0070}$	$(4d)^{29.9320}$	$(5p)^{0.0529}$
	$Ag_3^{+}{}_{after}$	$(5s)^{2.1199}$	$(4d)^{29.9232}$	$(5p)^{0.0681}$
	$Ag_3^{+}{}_{\Delta}$	**$(5s)^{0.1130}$**	**$(4d)^{-0.0088}$**	**$(5p)^{0.0078}$**
	Xe_{Δ}	**$(5p)^{-0.1044}$**	**$(5d)^{0.0029}$**	
Ag_4^{+}+Xe	$Ag1_{before}$	$(5s)^{0.7289}$	$(4d)^{9.9712}$	$(5p)^{0.0419}$
	$Ag1_{after}$	$(5s)^{0.7848}$	$(4d)^{9.9687}$	$(5p)^{0.0422}$
	$Ag1_{\Delta}$	**$(5s)^{0.0559}$**	**$(4d)^{-0.0024}$**	**$(5p)^{0.0003}$**
	$Ag_4^{+}{}_{before}$	$(5s)^{2.9904}$	$(4d)^{39.8968}$	$(5p)^{0.1075}$
	$Ag_4^{+}{}_{after}$	$(5s)^{3.0951}$	$(4d)^{39.8914}$	$(5p)^{0.1128}$
	$Ag_4^{+}{}_{\Delta}$	**$(5s)^{0.1048}$**	**$(4d)^{-0.0054}$**	**$(5p)^{0.0054}$**
	Xe_{Δ}	**$(5p)^{-0.0967}$**	**$(5d)^{0.0026}$**	

as Ag1 in Figure 2.5 is listed in Table 2.4. The total electronic configuration for the silver cluster is defined as the summation of the electron occupancies of all the atoms in the silver cluster and is also reported. For Xe, only the differences in the Xe electron occupancy upon adsorption are shown.

Increasing the cluster size from monatomic Ag^+ to Ag_4^+, the equilibrium distance R_e increases from 2.87 to 3.06 Å, while the binding energy decreases from 73.91 to 27.62 kJ/mol and the σ donation decreases from 0.1470 to 0.0970 electron received by the silver cluster. Similar to the Xe–Ag^+ system, the d_π-d_π back-donation can be extended as the total loss of electron in the 4d orbital in all silver atoms of the cluster. NBO analysis shows that the d_π-d_π back-donation is negligible compared with the σ donation. For instance, for Xe–Ag_2^+ compound, the magnitude of electron transfer in the σ donation and the d_π-d_π back-donation are 0.117 and 0.006 electron, respectively. The correlations between the cluster sizes, the electron transfers and the binding energies are shown in Figure 2.6.

The decrease in the binding energy of Xe as the Ag_n^+ cluster size increase is due to the charge delocalization effect. The +1 charge is distributed over all silver atoms of the cluster. As a result, the electron occupancy of Ag's 5s orbital increases with the cluster size. Such higher electron occupancy in the Ag's 5s orbital hinders electron transfer from the Xe's 5p orbital to these orbitals. Consequently, as the cluster size increases, smaller number of electron is transferred from Xe to the silver cluster, leading to weaker binding energy.

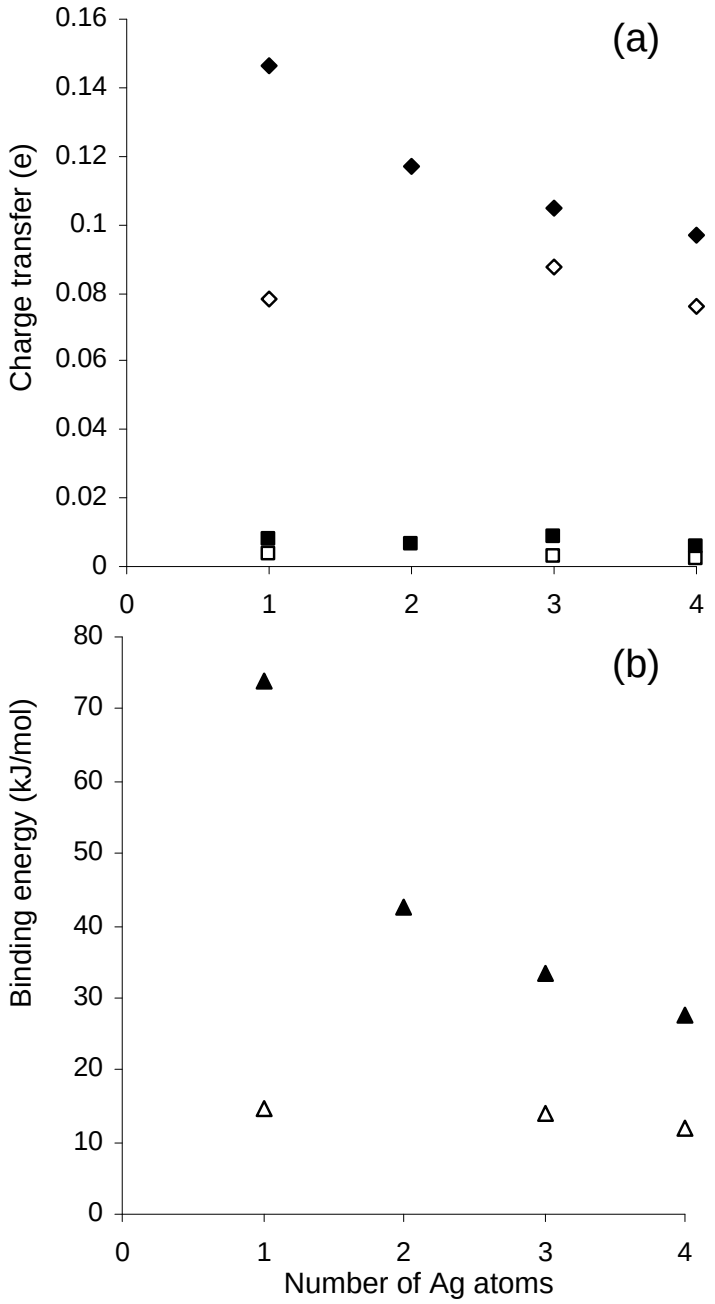

Figure 2.6 Correlation between binding energy, charge transfer and cluster size. (a) Magnitude of the σ donation (◆, ◇) and the d_π-d_π back-donation (■, □); (b) Binding energies of xenon and ionic silver clusters (▲, △). Filled markers are for gas phase silver clusters; unfilled markers are for silver clusters on chabazite surface.

2.3.2 Chabazite Surface

2.3.2.1 $Ag_{1,3,4}^{+}$ Clusters on The (001) Chabazite Surface

The structures of silver cluster cations on the 6T ring of the (001) chabazite surface were optimized with the seed of an Ag+ at the center of the ring. Silver clusters with 1, 3 and 4 Ag atoms were found to be stable whereas dimer Ag_2^+ was not at this site. Unlike the isolated Ag_4^+ cluster, Ag_4^+ on the chabazite surface has a tetrahedral configuration instead of a planar one. Upon binding with xenon, all of the silver cluster structures remain nearly the same. We found that adsorption of Xe has an insignificant effect on the structures of the adsorbed silver clusters. For simplicity, only the optimized structures of the silver clusters with xenon are shown in Figure 2.7.

The charges of silver clusters in Figure 2.7 reveal the electronic effect of the chabazite surface on the adsorbed silver clusters. The total charges of silver clusters and the surface are also given. The surface charge is the charge of the $[Si_7AlO_{16}H_{14}]$ quantum cluster. We found that there are dramatic differences in the electronic structures of Ag^+[Cha] as compared to those of Ag_3^+ and Ag_4^+. In particular, for the Ag^+[Cha] system, 0.1478 electron is transferred from [Cha] to Ag^+, making Ag^+ cation less positive than its original +1 charge. There is a total 0.1581 electron in the 5s orbital of Ag^+ as listed in Table 2.5. In contrast to the Ag^+[Cha] system, Ag_3^+ and Ag_4^+ transfer more than 0.6 electron to the zeolite surface upon adsorption, becoming more positive, specifically 1.6561 and 1.6163, respectively. This is because the additional Ag atoms are close to the O atoms of the 6T ring, which have higher electron affinity than Ag. Consequently, Ag_3^+ and Ag_4^+ on the surface have less electron in the 5s orbitals compared with their gas phase counterparts. For instance, the total number of electrons in the 5s orbitals of Ag_3^+

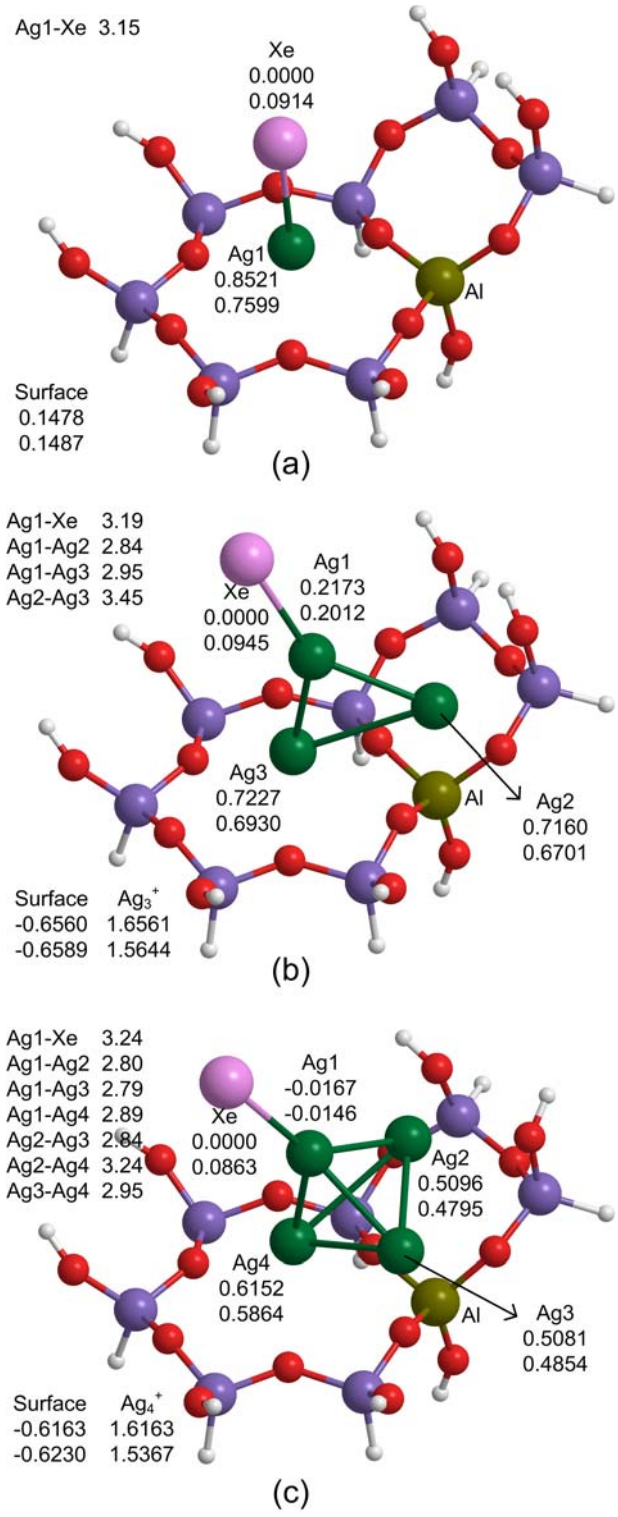

Figure 2.7 Xenon binding on ionic $Ag_{1,3,4}$ clusters on chabazite surface. Natural charges obtained from NBO analysis are showed under every atomic symbol. The first number is before binding and the second is after binding. The charge of the $[Si_7AlO_{16}H_{14}]$ quantum cluster is considered as the surface charge. Distances (Å) between silver and xenon atoms are shown.

Table 2.5 Binding Energy D_e (kJ/mol) and Equilibrium Distance R_e (Å) of Xe and Ionic $Ag_{1,3,4}^+$ Clusters on Chabazite Surface

	D_e	R_e
Ag_1^+	14.53	3.15
Ag_3^+	14.11	3.19
Ag_4^+	11.82	3.24

in gas phase and on the zeolite surface are 2.0070 and 1.3500 electrons, respectively. This suggests that such differences may lead to very a different binding energy for Xe on Ag^+ and on larger clusters.

2.3.2.2 Xenon Binding with $Ag_{1,3,4}^+$ Clusters on (001) Chabazite Surface

The cation silver clusters on the chabazite surface lose part of their affinity for xenon compared to their isolated counterparts. Results of binding energies are shown in Figure 2.6 and Table 2.5. The binding energy D_e declines and the equilibrium distance R_e increases when the cluster size increases. Analysis of natural atomic orbital occupancies in Table 2.6 provides insight into this loss of Xe affinity. The appearance of 0.1581 electron in the Ag's 5s orbital in the Xe–Ag+[Cha] system causes a reduction in the charge transfer from 0.146 in isolated Xe–Ag+ to 0.067 electron. The binding energy decreases significantly from 73.91 to 14.53 kJ/mol.

There are large gaps in the binding energies of Xe with isolated Ag+ and Ag3,4+. However, on the chabazite surface, the binding energies are much closer and are 14.53, 14.11, and 11.82 kJ/mol, respectively (Figure 2.6). These values are smaller than our experimental estimate of 42 kJ/mol.[13] Furthermore, the results are in fact counter-intuitive with the calculated total charges of the adsorbed Ag clusters mentioned above.

Table 2.6 B3LYP/LANL NAO Electron Occupancies of $Ag_{1,3,4}^{+}$ Clusters on Chabazite Surface and Xe Before and After Binding

Ag^{+}+Xe	$Ag1_{before}$	$(5s)^{0.1581}$	$(4d)^{9.9531}$	$(5p)^{0.0240}$
	$Ag1_{after}$	$(5s)^{0.2251}$	$(4d)^{9.9663}$	$(5p)^{0.0310}$
	$Ag1_{\Delta}$	**$(5s)^{0.0670}$**	**$(4d)^{0.0132}$**	**$(5p)^{0.0070}$**
	Xe_{Δ}	**$(5p)^{-0.0784}$**	**$(5d)^{0.0033}$**	
Ag_3^{+}+Xe	$Ag1_{before}$	$(5s)^{0.7737}$	$(4d)^{9.9849}$	$(5p)^{0.0063}$
	$Ag1_{after}$	$(5s)^{0.7800}$	$(4d)^{9.9810}$	$(5p)^{0.0095}$
	$Ag1_{\Delta}$	**$(5s)^{0.0062}$**	**$(4d)^{-0.0039}$**	**$(5p)^{0.0032}$**
	$Ag_3^{+}{}_{before}$	$(5s)^{1.3500}$	$(4d)^{29.8797}$	$(5p)^{0.0874}$
	$Ag_3^{+}{}_{after}$	$(5s)^{1.4298}$	$(4d)^{29.8743}$	$(5p)^{0.1040}$
	$Ag_3^{+}{}_{\Delta}$	**$(5s)^{0.0799}$**	**$(4d)^{-0.0053}$**	**$(5p)^{0.0166}$**
	Xe_{Δ}	**$(5p)^{-0.0878}$**	**$(5d)^{0.0026}$**	
Ag_4^{+}+Xe	$Ag1_{before}$	$(5s)^{0.9831}$	$(4d)^{9.9731}$	$(5p)^{0.0607}$
	$Ag1_{after}$	$(5s)^{0.9829}$	$(4d)^{9.9696}$	$(5p)^{0.0580}$
	$Ag1_{\Delta}$	**$(5s)^{-0.0002}$**	**$(4d)^{-0.0024}$**	**$(5p)^{-0.0027}$**
	$Ag_4^{+}{}_{before}$	$(5s)^{2.3120}$	$(4d)^{39.8566}$	$(5p)^{0.1773}$
	$Ag_4^{+}{}_{after}$	$(5s)^{2.3859}$	$(4d)^{39.8518}$	$(5p)^{0.1854}$
	$Ag_4^{+}{}_{\Delta}$	**$(5s)^{0.0739}$**	**$(4d)^{-0.0048}$**	**$(5p)^{0.0080}$**
	Xe_{Δ}	**$(5p)^{-0.0762}$**		**$(5d)^{0.0022}$**

The larger positive charge on the adsorbed Ag3,4+ clusters indicates the larger degree of vacancy in their 5s orbitals. From the above discussion, this would suggest the larger degree of σ donation and thus larger binding energy. The results confirm that the σ donation of Xe on the adsorbed Ag+ is smaller than that of the adsorbed Ag3+ (0.0784 < 0.0878). Closer examination reveals that the binding energy of Xe to Agn+ clusters depends more closely on the occupancy of the Ag1 atom that binds directly with Xe rather than the total charge of the cluster and the degree of charge transfer from Xe to that atom upon adsorption. Unlike Ag1 in the isolated Ag3,4+ clusters, which receive almost half of the σ donation, Ag1 in the adsorbed Ag3+[Cha] gets only 8% of the total charge transfer from Xe upon adsorption. In Ag4+[Cha], the charge of Ag1 is almost unchanged after binding with Xe (from -0.0167 to -0.0146 in Figure 2.7). A large part of the charge transfer from Xe goes to other silver atoms that bind directly to the zeolite surface. In Ag3,4+ clusters in Figure 2.7, the changes in charge of Ag1 are less significant than those of others. Consequently, the small changes in the Ag1 charge upon adsorption provide an explanation for the small differences in the Xe binding energies.

2.3.2.3 Xenon Binding with Neutral $Ag_{1,3,4}$ and Na^+ Clusters on (001) Chabazite Surface

For completeness, the interaction of xenon with reduced silver clusters on the chabazite surface was also studied. No binding with xenon was found on any size of neutral silver clusters. The inert behavior of the reduced Ag-chabazite is in agreement with our experimental observation and those of others.[6]

Adsorption of Xe on the Na^+[Cha] was also studied for comparison with Xe on Ag^+[Cha]. The calculated binding energy of Xe on Na^+[Cha] is 7.17 kJ/mol, which is

smaller than that of Ag^+[Cha] because of the difference in size between 3s and 5s orbitals. This value is also smaller than that of free Na^+. Without the charge transfer from chabazite, the 3s orbital of isolated Na^+ is more susceptible to electron transfer from Xe's 5p orbital.

Finally, all the silver clusters in our study, free or bound to the chabazite surface, follow a pattern – increase in the cluster size leads to diminishing xenon binding strength. In the isolated clusters, Ag^+ is the most attractive. On the chabazite surface, Ag^+ has slightly larger Xe binding affinity compared to larger clusters. It is possible to extrapolate this trend to nanoparticles in the order of about 20 silver atoms as in the experiment shown Figure 2.1.

2.4 Discussion

2.4.1 Correlation Between σ Donation and Xe Binding Properties

Traditionally, interaction between Xe and Ag_n^+ can be described by the attractive charge-induced polarization and the van der Waals repulsion. Bellert and Breckenridge[42] introduced a model potential for monatomic cations and noble gases consisting of attractive terms with dependence on distance R ranging from $1/R^4$ to $1/R^8$ and an Ae^{-bR} repulsive term. Unfortunately, these potential functions rely on point charges and thus are not readily applicable for clusters where charge delocalization occurs. To provide further insight into interaction between Xe on adsorbed Ag_n^+ on the chabazite surface, the correlations between the binding energy with the equilibrium Xe-Ag bond distance with the σ donation are plotted in Figures 2.8 and 2.9, respectively. Note that the binding energy correlates well with the binding distance and the degree of σ donation. As the

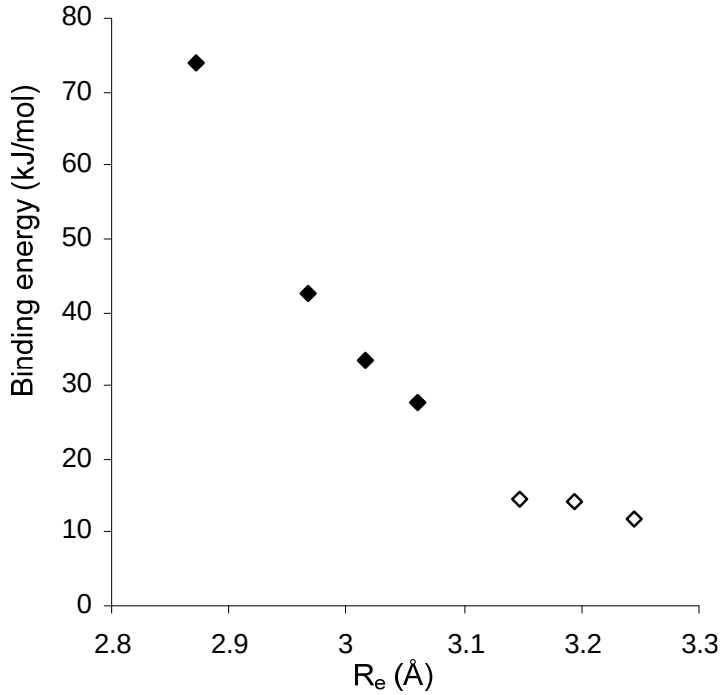

Figure 2.8 Binding energy of $Xe–Ag_n^+$ system versus the magnitude of the σ donation. Filled markers are for gas phase silver clusters; unfilled markers are for silver clusters on the chabazite surface.

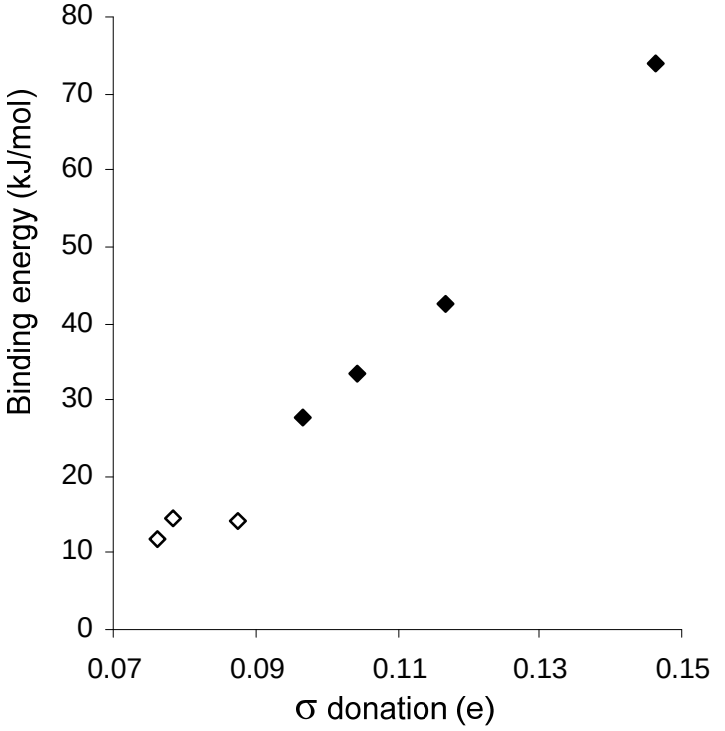

Figure 2.9 Binding energy of $Xe–Ag_n^+$ system versus the equilibrium distance. Filled markers are for gas phase silver clusters; unfilled markers are for silver clusters on the chabazite surface.

binding distance decreases, the overlap between the Ag's 5s and Xe's 5p orbitals increases leading to larger σ donation and consequently larger binding energy. The present study found that the zeolite framework can greatly reduce the Xe binding capability of Ag_n^+ clusters. This suggests that the effects of the zeolite framework are needed for investigating the potential use of zeolite in Xe separation.

2.4.2 Chemical Shifts

In this study, the d_π-d_π back-donation is negligible and therefore cannot be used to account for the unusual negative shifts in the ^{129}Xe NMR experiments on AgX and AgY zeolites. These shifts were first explained by the shielding effect formed by the d_π-d_π back-donation from Ag^+'s 4d orbital to Xe's 5d orbital by Gedeon et al.[6] However, *ab initio* calculation on gas phase Ag^+ and Xe by Freitag et al.[14] indicated that the shielding effect is attributable to the mixing between the 5p, 4p and 3p orbitals of Xe with the 4d orbitals of Ag^+. In the study by Freitag et al., the ^{129}Xe NMR chemical shift curve for Xe–Ag^+ shows two regions: (1) positive shift due to the deshielding polarization of the Xe charge distribution by Ag^+ when Xe–Ag^+ distance is greater than 3.7 Å and (2) negative shift due to the exponentially increasing shielding contributions of the p orbitals at Xe by mixing with Ag^+'s d orbitals when Xe–Ag^+ distance is smaller than 3.7 Å. Using Mulliken analysis, Freitag et al. did not find any d_π-d_π back-donation but instead the electron transfer from the p orbitals of Xe to the s and p orbitals of Ag^+. Results of Freitag et al. were later confirmed by the work of Moudrakovski et al. and Jameson et al. on AgA zeolite.[15,16] According to these authors, Xe atoms are physisorbed rather than greater than 3.7 Å, giving positive chemical shift, could easily overwhelm the negative contributions from less than 3.7 Å configurations.

For small ionic silver clusters in the gas phase and on the (001) chabazite surface, the σ donation is far more dominant than the d_π-d_π back-donation, resulting in a total charge transfer from xenon to silver. Our results of the Xe binding distances in Table 2.5 are less than 3.7 Å and thus suggest the observed negative NMR shifts are due to adsorption of Xe on small Ag_n^+.

2.5 Summary

We presented a computational study of the adsorption of xenon on gas phase silver clusters (n = 1-4 atoms) and on the silver-exchanged chabazite surface using cluster models. The binding between xenon and silver, in essence, is the σ donation which is the charge transfer from the 5p orbital of xenon to the 5s orbital of silver. Our results prove that Ag_{1-4} clusters have the enhanced affinity for xenon but only in the ionic state because of the empty Ag's 5s orbitals. When reduced to neutral, these silver clusters show no Xe affinity. Increasing the size of cation clusters in our computational model weakens the xenon adsorption because of the delocalization of the positive charge. The ionic gas phase silver clusters bind xenon much more strongly than those adsorbed on the chabazite surface. We found a strong correlation between the binding energy and the σ donation. The results indicate the d_π-d_π back-donation plays an insignificant role in Xe binding. Using the binding distance as an argument for physisorption or chemisorption, our results suggest the observed negative NMR chemical shift is from Xe adsorption on small Ag_n^+ clusters.

2.6 References

(1) Goto, T. *Can. J. Anesth.* **2002**, *49*, 335.

(2) Ito, T.; Fraissard, J. *J. Chem. Phys.* **1982**, *76*, 5225.

(3) Häussinger, P.; Glatthaar, R.; Rhode, W.; Kick, H.; Benkmann, C.; Weber, J. In *Ullmann's Encyclopedia of Industrial Chemistry*; Wiley: 2001.

(4) Jeanes, T. O.; Jensvold, J. A. 2001.

(5) Fraissard, J.; Gedeon, A.; Chen, Q.; Ito, T. *Stud. Surf. Sci. and Catal.* **1991**, *69*, 461.

(6) Gedeon, A.; Burmeister, R.; Grosse, R.; Boddenberg, B.; Fraissard, J. *Chem. Phys. Lett.* **1991**, *179*, 191.

(7) Grosse, R.; Burmeister, R.; Boddenberg, B.; Gedeon, A.; Fraissard, J. *J. Phys. Chem.* **1991**, *95*, 2443.

(8) Gedeon, A.; Fraissard, J. *Chem. Phys. Lett.* **1994**, *219*, 440.

(9) Grosse, R.; Gedeon, A.; Watermann, J.; Fraissard, J.; Boddenberg, B. *Zeolites* **1992**, *12*, 909.

(10) Watermann, J.; Boddenberg, B. *Zeolites* **1993**, *13*, 247.

(11) Munakata, K.; Kanjo, S.; Yamatsuki, S.; Koga, A.; Ianovski, D. *J. Nucl. Sci. Technol.* **2003**, *40*, 695.

(12) Kuznicki, S. M.; Anson, A.; Koenig, A.; Kuznicki, T. M.; Haastrup, T.; Eyring, E. M.; Hunter, D. *J. Phys. Chem. C* **2007**, *111*, 1560.

(13) Konya, G.; Eyring, E. M.; Hunter, D., unpublished work., University of Utah, USA.

(14) Freitag, A.; van Wüllen, C.; Staemmler, V. *Chem. Phys.* **1995**, *192*, 267.

(15) Moudrakovski, I. L.; Ratcliffe, C. I.; Ripmeester, J. A. *J. Am. Chem. Soc.* **1998**, *120*, 3123.

(16) Jameson, C. J.; Lim, H.-M. *The Journal of Chemical Physics* **1997**, *107*, 4373.

(17) Kuznicki, S. M.; Kelly, D. J. A.; Bian, J.; Lin, C. C. H.; Liu, Y.; Chen, J.; Mitlin, D.; Xu, Z. *Micro. Meso. Mater.* **2007**, *103*, 309.

(18) Glendening, E. D.; Badenhoop, J. K.; Reed, A. E.; Carpenter, J. E.; Bohmann, J. A.; Morales, C. M.; Weinhold, F. 2001.

(19) Chen, N.; Yang, R. T. *Ind. Eng. Chem. Res.* **1996**, *35*, 4020.

(20) Huda, M. N.; Ray, A. K. *Eur. Phys. J.* **2003**, *22*, 217.

(21) Wang, Y.; Gong, X. G. *Eur. Phys. J.* **2005**, *34*, 19.

(22) Baerlocher, C.; McCusker, L. B.

(23) Hill, J.; Subramanian, L.; Maiti, A. *Molecular Modeling Techniques in Material Sciences*; Taylor & Francis, 2005.

(24) Calligaris, M.; Mezzetti, A.; Nardin, G.; Randaccio, L. *Zeolites* **1984**, *4*, 323.

(25) Calligaris, M.; Nardin, G.; Randaccio, L. *Zeolites* **1983**, *3*, 205.

(26) Johnson, E. R.; Wolkow, R. A.; DiLabio, G. A. *Chem. Phys. Lett.* **2004**, *394*, 334.

(27) Pérez-Jordá, J. M.; Becke, A. D. *Chem. Phys. Lett.* **1995**, *233*, 134137.

(28) Yousef, A.; Shrestha, S.; Viehland, L. A.; Lee, E. P. F.; Gray, B. R.; Ayles, V. L.; Wright, T. G.; Breckenridge, W. H. *J. Chem. Phys.* **2007**, *127*, 154309.

(29) Koga, T.; Tatewaki, H.; Shimazaki, T. *Chemical Physics Letters* **2000**, *328*, 473.

(30) Osanai, Y.; Sekiya, M.; Noro, T.; Koga, T. *Molecular Physics* **2003**, *101*, 65.

(31) Simon, S.; Duran, M.; Dannenberg, J. J. *J. Chem. Phys.* **1996**, *105*, 11024.

(32) Chalasinski, G.; Szczesniak, M. M. *Chem. Rev.* **2000**, *100*, 4227.

(33) Treesukol, P.; Limtrakul, J.; Truong, T. N. *J. Phys. Chem. B* **2001**, *105*, 2421.

(34) Stefanovich, E. V.; Truong, T. N. *J. Phys. Chem. B* **1998**, *102*, 3018.

(35) Jungsuttiwong, S.; Khongpracha, P.; Truong, T. N.; Limtrakul, J. *Stud. Surf. Sci. and Catal.* **2001**, *135*, 2518.

(36) Jungsuttiwong, S.; Limtrakul, J.; Truong, T. N. *J. Phys. Chem. B* **2005**, *109*, 13342.

(37) Khaliullin, R. Z.; Bell, A. T.; Kazansky, V. B. *J. Phys. Chem. A* **2001**, *105*, 10454.

(38) Treesukol, P.; Kanokthip, S.; Jumras, L.; Truong, T. N. *J. Phys. Chem. B* **2005**, *109*, 11940.

(39) Gaussian 03, R. C., Frisch, M. J.; Trucks, G. W.; Schlegel, H. B.; Scuseria, G. E.; Robb, M. A.; Cheeseman, J. R.; Montgomery, Jr., J. A.; Vreven, T.; Kudin, K. N.; Burant, J. C.; Millam, J. M.; Iyengar, S. S.; Tomasi, J.; Barone, V.; Mennucci, B.; Cossi, M.; Scalmani, G.; Rega, N.; Petersson, G. A.; Nakatsuji, H.; Hada, M.; Ehara, M.; Toyota, K.; Fukuda, R.; Hasegawa, J.; Ishida, M.; Nakajima, T.; Honda, Y.; Kitao, O.; Nakai, H.; Klene, M.; Li, X.; Knox, J. E.; Hratchian, H. P.; Cross, J. B.; Bakken, V.; Adamo, C.; Jaramillo, J.; Gomperts, R.; Stratmann, R. E.; Yazyev, O.; Austin, A. J.; Cammi, R.; Pomelli, C.; Ochterski, J. W.; Ayala, P. Y.; Morokuma, K.; Voth, G. A.; Salvador, P.; Dannenberg, J. J.; Zakrzewski, V. G.; Dapprich, S.; Daniels, A. D.; Strain, M. C.; Farkas, O.; Malick, D. K.; Rabuck, A. D.; Raghavachari, K.; Foresman, J. B.; Ortiz, J. V.; Cui, Q.; Baboul, A. G.; Clifford, S.; Cioslowski, J.; Stefanov, B. B.; Liu, G.; Liashenko, A.; Piskorz, P.; Komaromi, I.; Martin, R. L.; Fox, D. J.; Keith, T.; Al-Laham, M. A.; Peng, C. Y.; Nanayakkara, A.; Challacombe, M.; Gill, P. M. W.; Johnson, B.; Chen, W.; Wong, M. W.; Gonzalez, C.; and Pople, J. A.; Gaussian, Inc., Wallingford CT, 2004.

(40) Brock, L. R.; Duncan, M. A. *J. Chem. Phys.* **1995**, *103*, 9200.

(41) Kalus, G.; Litzén, U.; Launay, F.; Tchang-Brillet, W.-U. L. *Phys. Scr.* **2002**, *65*, 46.

(42) Bellert, D.; Breckenridge, W. H. *Chem. Rev.* **2002**, *102*, 1595.

CHAPTER 3

THEORETICAL STUDY ON THE INTERACTION BETWEEN XENON AND TRANSITION METAL CATIONS OF GROUP 10, 11, AND 12

3.1 Introduction

In the previous chapter, silver-exchanged chabazite was studied as the promising materials for xenon separation. To bind xenon, the virtual 5s orbital of Ag^+ is the necessity. In the gas phase, the binding between Xe and Ag^+ is because of the σ donation, which is the electron transfer from the 5p orbital of xenon to the empty s orbital of the Ag^+.[1,2] Because other cations of group 11 (Cu^+ and Au^+) share the s^0 configuration with Ag^+, this mechanism also applies to the gas-phase Ag^+–Xe and Au^+–Xe complexes. In zeolite structures, our theoretical study on xenon and small silver clusters doped on chabazite surface shows that the exact mechanism is observed although in a lesser extent due to the increase in size of the silver clusters and the effect of the chabazite surface.[3] The fact that the σ donation is the xenon binding mechanism for gas-phase Cu^+, Ag^+, and Au^+ and for Ag^+ in chabazite leads to the idea of using Cu-exchanged and Au-exchanged zeolites as possible materials to capture xenon. Moreover, the xenon binding strengths of Cu, Ag, and Au-exchanged zeolites may be deduced from the order of strength of their respective gas-phase cations.

Interestingly, Ag^+ is not the most attractive transition metals to xenon in the gas phase. This conclusion can be drawn from the several recent theoretical works on the

transition metals in group 11 and 12 with xenon.[4-6] Of the 6 transition metals in group 11 and 12, Ag^+ comes after Au^+ and Cu^+ in binding with xenon. However, this is against the widely usage of silver-exchanged materials by experimentalists.[7-10] Resolving this contradiction requires better understanding on xenon and transition metals, both in the gas phase and in the zeolite structures.

In the gas phase, there has been considerable interest in chemistry of noble gases and ions complexes. This is because the solvation of ions is important in many areas, from inorganic chemistry, electrochemistry to biochemistry; and the rare gas atoms can serve as the simplest solvents. These interactions have been studied both experimentally and theoretically. An excellent review on ion–Rare gas interactions was written by Bellert and Breckenridge in 2002.[11] After that, the focus has shifted to the heavy alkali and transition metal cations with heavy Rg.[4-6,12-21] Since the pioneer work of Pyykkö[2,22] on Au^+–Xe in 1995, there has been very little theoretical work on these heavy systems, probably owing to the large number of electrons one has to deal with. For the systems of interest in this study, Yousef et al. conducted a thorough study on coinage metals in group 11 and noble gases.[6] The transition metals of group 12 were covered by Lee et al. and Qing et al.[4,5] Au^+–Xe is the strongest ion–Rare gas known up to date and received special attention with other recent studies by Belpassi et al., Zeng and Klobukowski, and Breckenridge et al.[19-21] However, for group 10, there were only studies on Ni^+ and Pt^+ with rare gases from He to Ar.[23,24] Several studies on neutral systems of Ni, Pd, Pt–Rare gas were also conducted.[14,16,25] Besides the probable lack of needs, we can only speculate that the minimal attention cationic Ni, Pd and Pt received is due to the difficulties arising with theoretical calculations. Complexes of cationic Ni, Pd, Pt and noble gases are open-

shell compounds which are hard to converge compared with closed-shell systems of group 11 like M^+–Rare gas or Rare gas-MX (M = Cu, Ag, Au; X = F, Cl).[6,18] Moreover, one needs to account for the spin-orbit effect in group 10. The SO effect can be ignored in group 11 and 12 because the energy levels of ground states and excited states are far apart. This effect is pronounced in group 10 because of the low lying excited states resulted from the appearance of the open d orbitals. These difficulties reflect the differences between these groups. Firstly, the cations of group 11 have a full d space and an empty s space $(n\text{-}1)d^{10}ns^0$ while those of group 12 have $(n\text{-}1)d^{10}ns^1$ configurations. So the σ donation is weakened in group 12. Secondly, the cations of group 10 have nd^9 configurations. One can reason that the open d orbital can stabilize M^+–Xe complexes by accepting electrons to form a dative bond. Therefore, it can be inferred that cations of group 10 would bind xenon better than those of group 11 and 12.

The effects of relativity are important for systems with transition metals, especially the ones in row 6. In Pyykkö's study on Au^+–Xe, half of the binding energy comes from the relativistic effect.[2] Some literatures also show that when moving vertically in the periodic table, bond lengths of transition metal compounds vary anomalously. For example, experimental work on metal–carbon bond length in group 12 dimethyl compounds showed an increase in bond length from Zn to Cd, but a decrease from Cd to Hg, although the expected trend was an increase from Zn to Cd then to Hg.[26] The same pattern was observed in the bond lengths of Cu^+, Ag^+, and Au^+–Xe in Yousef et al.'s work.[6] The decreases in bond length in these two studies are caused by the fact that the 6s shells of Au and Hg are strongly contracted by the relativistic effects. There are two methods to include these effects in *ab initio* calculations and they were both used in this

study. The first is the scalar and spin-orbit Douglas-Kroll approximation used for all-electron calculation.[27] In the second method, both scalar relativistic effects and spin-orbit (SO) effects are included in the effective core potential (ECP) which was used to replace the core electrons of atoms.

In the present work, we carried out a systematic theoretical study on the interactions in the gas phase of xenon with Ag^+ and other metals surrounding it, which are the nine transition metals of group 10, 11, and 12 – Ni^+, Pd^+, Pt^+, Cu^+, Ag^+, Au^+, Zn^+, Cd^+, and Hg^+. The objective of this study was to provide a comprehensive insight into the mechanisms of these interactions, i.e., how the differences in electronic structure of transition metal cations correlate with the binding strengths as well as how the relativity affects the binding. Knowledge of these gas-phase interactions is the first step toward understanding the binding between xenon and metal-exchanged zeolite. The nature of the ion–Xe complexes was studied using the natural bond orbital (NBO) analysis.[28] However, a definite description of these interactions is hard to achieve because of the complexity of these bindings. For instance, after spending the many efforts in more than 10 years to study gold ion and xenon, researchers have just reached a consensus about the covalent nature of their interaction.[19-21] Here we focused on studying the charge transfer between the 5p orbital of xenon and the *n*s orbital of M^+ and the contribution of (*n*-1)d and *n*p orbitals of M^+ to the interactions.

3.2 Methodology

In this study, three types of basis sets from different laboratories were employed. The first is the Sapporo all-electron basis set.[29-33] The second and third are the Karlsruhe[34] and the Stuttgart BSs[35-39] with relativistic ECPs. The Karlsruhe ECP can

account for scalar relativistic effects. The Stuttgart ECP is the two-component (scalar and spin-orbit) relativistic pseudopotential. For Karlsruhe basis sets, we used all-electron basis sets for third row complexes and ECPs for fourth and fifth row ones. For Stuttgart basis set, all atoms except Ni were treated with ECPs. These ECPs are small-core potentials which treat 10 electrons as core ($1s^2 2s^2 2p^6$) for Cu and Zn, 28 electrons as core (up to 3d subshell) for Pd, Ag, Cd, and Xe and 60 electrons as core (up to 4f subshell) for Pt, Au, and Hg. There are several versions for the Stuttgart ECPs. We opted to use the most recent Stuttgart ECP28MDF and ECP60MDF in which MDF stands for multi-electron fit and fully relativistic. The largest size available for each basis set was chosen. The Sapporo and Karlsruhe basis sets were used at quadruple-ζ level while Stuttgart BSs at quintuple-ζ level (aug-cc-pV5Z). Pyykkö and Burda et al. stressed the importance of including g functions in the BSs for Au^+–Xe and Pt–Xe. All chosen BSs in this study satisfy this requirement. Sapporo and Karlsruhe contain from s to h functions. Stuttgart basis sets have i functions which were omitted in prior studies.[4-6] We decided to keep the Stuttgart basis sets in this study intact. For Ni^+–Xe, the all-electron relativistic third-order Douglas-Kroll approximation was employed.[40] Ni was treated with aug-cc-pV5Z basis set while Xe with Sapporo basis sets because there is no all-electron Stuttgart basis set for Xe. The contraction schemes of the basis sets and the ECPs of our and previous studies' basis sets are presented in Table 3.1.

It is useful to compare our methodology choices with previous studies. Without sacrificing accuracy, pseudopotential has been preferred for use in systems which would be difficult to deal with using all-electron basis set. Like us, Qing et al., Lee et al., Yousef et al., and Breckenridge et al. employed the Stuttgart ECPs in their studies on group 11,

Table 3.1 Comparison Between Basis Sets Used in This Study and in References

	Basis set	Contraction schemes	Pseudopotential
Ni, Cu, Zn	Sapporo	(25s13p11d4f2g)/[6s4p4d2f1g]	all-electron
	Karlsruhe	(24s18p10d4f2g)/[11s6p5d4f2g]	all-electron
Ni	Stuttgart	(29s21p13d5f4g3h2i)/[10s9p7d5f4g3h2i]	all-electron
Cu, Zn	Stuttgart	(17s14p13d5f4g3h2i)/[8s8p7d5f4g3h2i]	ECP10MDF
Cu	Yousef et al.[6]	(26s18p20d5f3g2h)/[8s6p6d5f3g2h]	ECP10MDF
Zn	Lee et al.[5]	same as Stuttgart	ECP10MDF
Pd, Ag, Cd	Sapporo	(23s16p18d3f2g)/[7s5p5d2f1g]	all-electron
	Karlsruhe	(10s8p7d4f2g)/[7s5p4d4f2g] (Ag 9s)	ECP-28
	Stuttgart	(17s14p12d5f4g3h2i)/[8s8p7d5f4g3h2i]	ECP28MDF
Ag	Yousef et al.[6]	(26s23p22d4f3g2h)/[8s7p6d4f3g2h]	ECP28MDF
Cd	Qing et al.[4]	[11s10p8d5f4g]	ECP28MWB

Table 3.1 (continued)

	Basis set	Contraction schemes	Pseudopotential
Pt, Au, Hg	Sapporo	(30s25p21d17f2g)/[8s6p7d3f1g]	all-electron
	Karlsruhe	(10s8p6d4f2g)/[7s5p4d4f2g] (Au 9s)	ECP-60
	Stuttgart	(17s14p12d5f4g3h2i)/[8s8p7d5f4g3h2i]	ECP60MDF
Au	Schröder et al[22]	(8s6p5d5f1g)/[7s3p4d5f1g]	ECP60MWB
	Zeng and Klobukowski[19]	(28s23p20d2f1g)/[5s3p7d2f1g]	MCP
	Yousef et al.[6]	(26s23p22d4f3g2h)/[8s7p6d4f3g2h]	ECP60MDF
Hg	Qing et al.[4]	[11s10p8d5f4g]	ECP60MWB
Xe	Sapporo	(21s18p14d2f2g)/[6s6p4d2f1g]	all-electron
	Karlsruhe	(11s10p8d2f)/[6s5p3d2f]	ECP-28
	Stuttgart	(17s14p14d4f3g2h)/[8s8p6d4f3g2h]	ECP28MDF
	Schröder et al[22]	(8s8p6d6f)/[7s7p6d6f]	ECP46MWB
	Zeng and Klobukowski[19]	(28s23p21d6f1g)/[6s5p5d6f1g]	MCP
	Yousef et al.[6]	same as Stuttgart	ECP28MDF
	Qing et al.[4]	[8s8p5d4f3g]	ECP28MDF

12 cations and noble gases.[4-6,21] While keeping the standard aug-cc-pV5Z BSs for noble gases, these authors developed different BSs at quintuple-ζ level for valence electrons of the cations. Until now, Stuttgart ECPs have evolved greatly from their original simple forms – from single to multi electron fit, from large core to small core, from non to quasi (not including SO effect) to fully relativistic (including SO effect). Pioneers in ion–Rg interaction research had to employ simple pseudopotentials due to the limitation of both computing resource and available pseudopotentials. However, advanced pseudopotentials are standard for recent studies. For instance, early study on Au^+–Xe by Schröder et al.[22] replaced core electrons of Xe by using ECP46MWB, which is large core (46 electrons) and quasi relativistic. This ECP is inferior to the small core (28 electrons) and fully relativistic ECP28MDF used by Yousef et al. and us for the same system. However, for Au and other transition metals of group 11 and 12, it turns out that the main advantage of the advanced ECP is the small core characteristic. That is because SO effects in group 11 and 12 are small so the differences from results from MWB and MDF ECP are negligible. Some researchers of the Yousef et al. group continue to conduct further study on the Au^+–Xe complex, in which they improved their calculations to achieve results at the BS limit.[21] Very accurate results were necessary for these authors to perform the model potential analyses to decide if the Au^+–Xe bonding is covalent or physical. As our main concern was more about relative comparison between the transition metals, our choice of basis sets and pseudopotentials is satisfactory for this study.

Besides ECP, another type of pseudopotential is the model core potentials (MCP). Zeng and Klobukowski used MCP to study Au^+–Xe complex.[19] They explained that their results could be an improvement compared with other ECP results because MCPs with

correct nodal structure better describe the vicinity of a nucleus, where the scalar-relativistic effects mainly take place. The MCPs of Zeng and Klobukowski replace more core electrons than the ECPs. The BSs of Zeng and Klobukowski are for 17 electrons for Au ($5p^6 5d^{10} 6s^1$) and 18 electrons for Xe ($4d^{10} 5s^2 5p^6$) while both Karlsruhe and Stuttgart BSs are for 19 electrons for Au ($5s^2 5p^6 5d^{10} 6s^1$) and 26 electrons for Xe ($4s^2 4p^6 4d^{10} 5s^2 5p^6$). Zeng and Klobukowski argued that because the order of orbital energies for Au atom is [core]5s4f5p5d6s, there is no reason to include the 5s subshell into the valence space while excluding 4f, as is the case of ECPs.

The Molpro quantum chemistry package was used for all calculations in this study.[41] All potential energy curves were obtained point by point at the coupled cluster (CC) level of theory with single and double excitation and with noniterative correction for triple excitations (CCSD(T) method). Being a high-level correlation method, CCSD(T) had been the standard for studies on transition metal cation – noble gas interactions.[2,4-6,19] The excited states of M^+–Xe (M in group 11 and 12) are far away enough in energy that one expects a single-reference method like CC is sufficient. However, the same argument cannot be applied for the TMs of group 10 because the excited states are closer to the ground state. To justify the use of CCSD(T) for group 10 in this study, the T1 diagnostic index was examined. The T1 diagnostic index is effective for judging whether a system is single-reference in nature or not. If T1 is smaller than 0.02, the use of single-reference is assumed to be safe. The largest T1 diagnostic indexes in this study are 0.016, 0.016, and 0.018 for Ni, Pd, and Pt, respectively. So the CC method is acceptable. To calculate the electron correlation energy with CCSD(T), the

$5s^2 5p^6$ electrons of xenon were correlated. For the transition metal cations, the outermost $(n\text{-}1)d^9$, $(n\text{-}1)d^{10}$, and $(n\text{-}1)d^{10}ns^1$ electrons were correlated, respectively.

Compared with other methods like Hartree-Fock (HF), second-order Møller-Plesset (MP2) perturbation, and density functional theory (DFT) methods, CC was shown to give better results. In the study of Zeng and Klobukowski on Au^+–Xe, HF, DFT, MP2 and CC theories were compared, and none of the other theories provided satisfactory results compared to CC.[19] MP2 was also found elsewhere to overestimate the correlation energy.[42] In our previous study, B3LYP DFT was employed to facilitate demanding calculation involving zeolite framework.[3] Although that choice of methodology was justified by a good reproduction of the Ag^+–Xe potential curve taken from CC studies, there is no guarantee that DFT can replace CC theory in a broader study on other TMs. Another work on Au^+–Xe worth mentioning here is of Belpassi et al.[20] They employed all-electron approaches which are the DC-CCSD(T) (DC means 4-component Dirac-Coulomb Hamiltonian that describes relativity without any approximation). These authors reasoned that the use of pseudopotentials on heavy nuclei may adversely affect the electron density analysis used to consider the covalency of Au^+–Xe, due to the lack of an explicit core-electron density.

Single-point calculations were carried out for internuclear distances ranging from 2.00 to 5.00 Å. Each point was corrected for the basis-set superposition error (BSSE) employing the full counterpoise correction.[43,44] To locate the minimum of the curves, calculations at distances with 0.01 Å increment around the equilibrium bond length were performed. From these internuclear distances and their potential energies, the LEVEL program[45] was used to obtain the dissociation energy and the rovibrational energy levels.

The NBO analysis was used to study the electronic structures of the M^+–Xe compounds.[28]

3.3 Results and Discussions

3.3.1 Potential Energy Curves

The potential curves from quintuple-ζ Stuttgart, quadruple-ζ Sapporo and Karlsruhe basis sets are presented in Figure 3.1 and Figure 3.2. Results from recent studies on group 11 and 12 are shown for comparison.[4-6,19] For group 10, our results appear to be the only ones available (Figure 3.1.a and Figure 3.2.a). From scanning the distance between Xe and M^+, 3 parameters of the potential curve are obtained. They are the equilibrium nuclear separation R_e, the depth of the potential well D_e, and the separation σ, at which the potential curve crosses through zero. As shown later, the results of Stuttgart BS were used to obtain the dissociation energy D_0, the vibrational constant ω_e, the anharmonicity constant $\omega_e x_e$, the rotational constant B_0, and the centrifugal distortion constant D_{J0}. All these spectroscopic parameters are presented in Table 3.2.

For group 11 and 12, from Figure 3.1.b, 3.1.c and Table 3.2, one can see that results from the three basis sets employed in this work are consistent and agree with previous studies. The largest discrepancy is of Cu^+–Xe. Sapporo, Karlsruhe, Stuttgart, and Yousef et al.'s D_e results for Cu^+–Xe are 7335, 7182, 7579 and 8301 cm^{-1}, respectively. Prior experimental investigations involving xenon are scarce. A couple of studies using photoionization spectroscopy estimated binding energies of Ag^+–Xe and Hg^+–Xe at >3900 and 6020±150 cm^{-1}, respectively.[46,47] Our D_e values with Stuttgart BS for these two species are 5943 and 5325 cm^{-1}. Like Qing et al., we could not offer a satisfactory explanation for the ~800 cm^{-1} difference with Hg^+–Xe's experimental D_e. Compared with

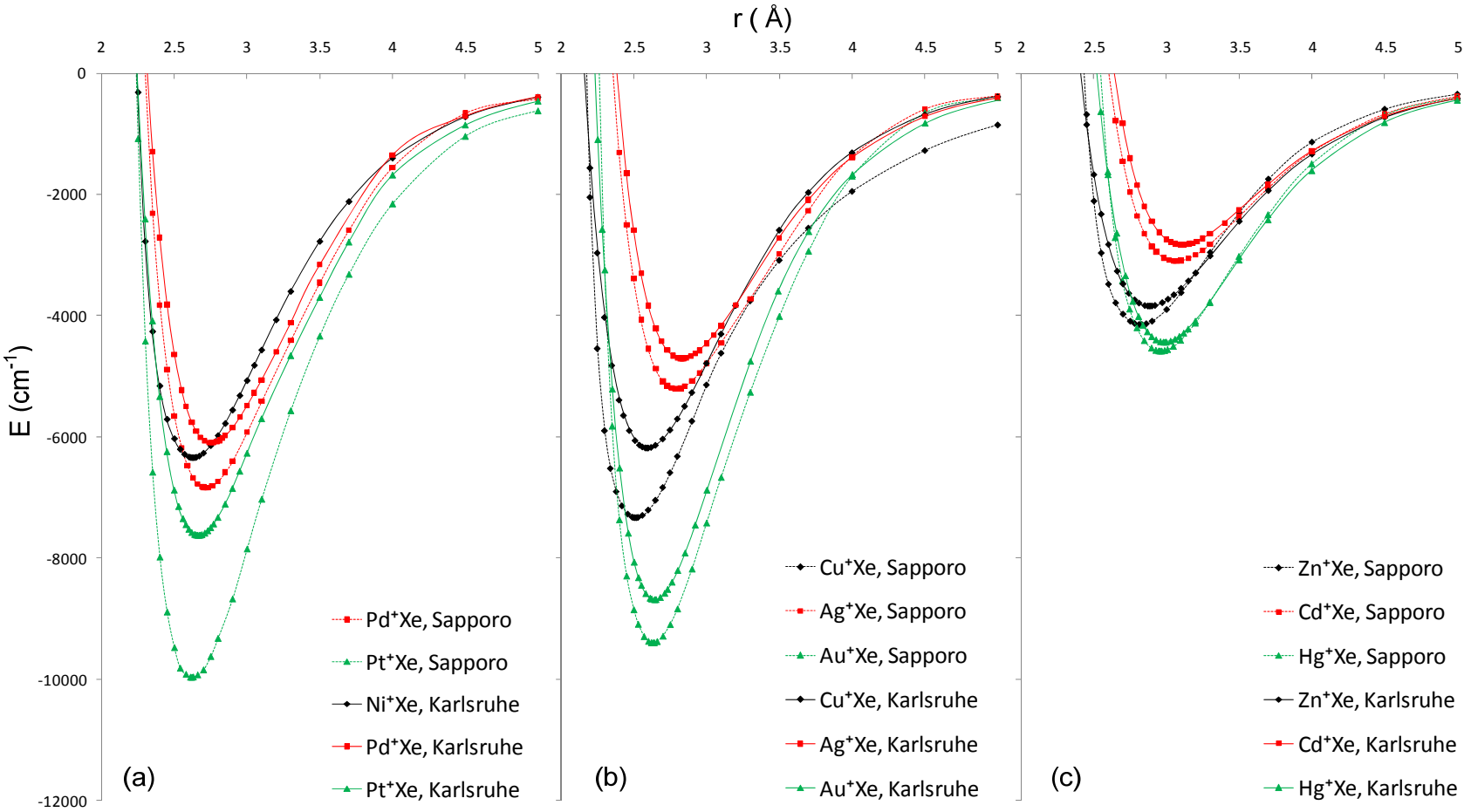

Figure 3.1 Potential energy curves for complexes of xenon and transition metal cations obtained with Sapporo and Karlsruhe basis sets. (a) group 10, (b) group 11, and (c) group 12.

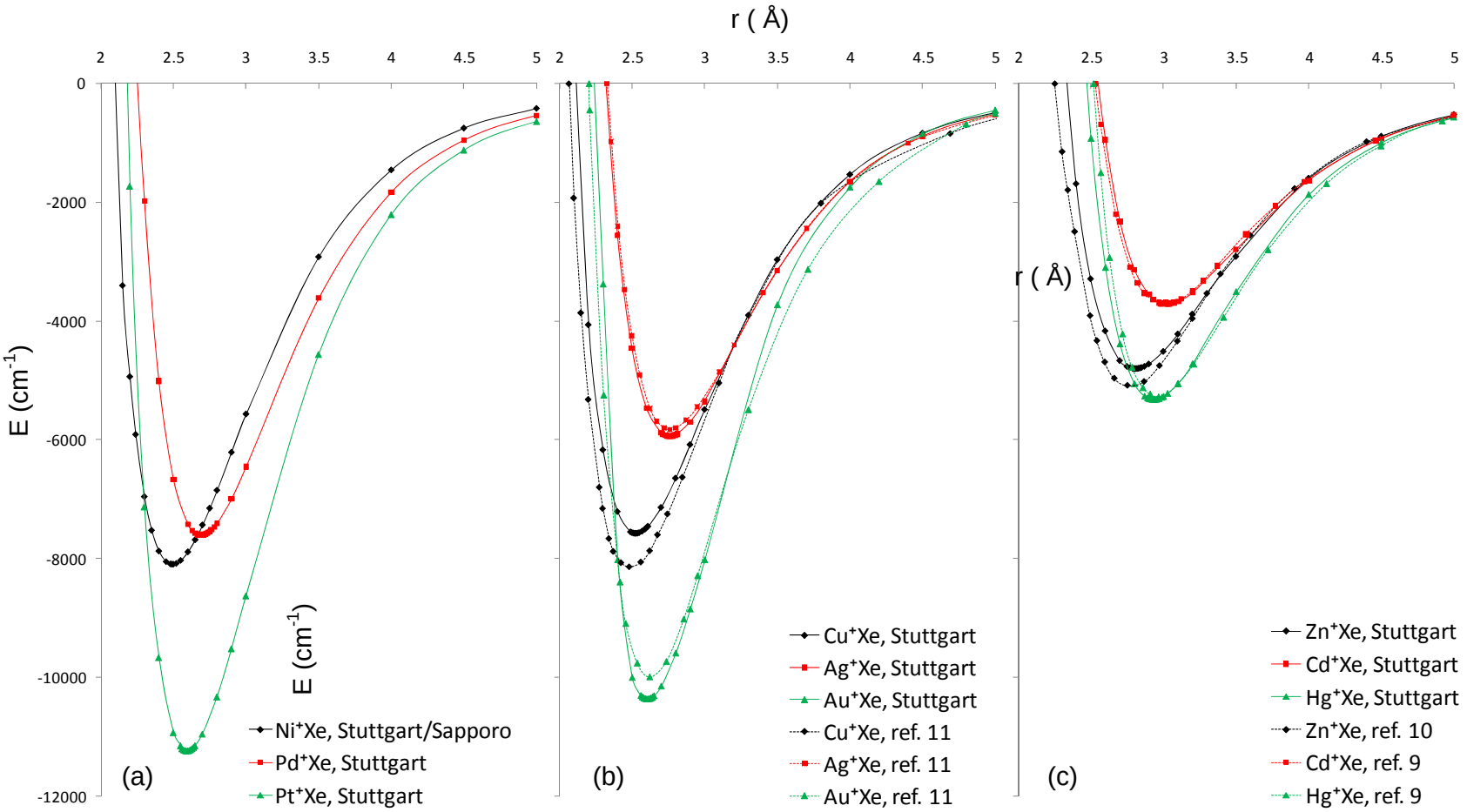

Figure 3.2 Potential energy curves for complexes of xenon and transition metal cations obtained with Stuttgart basis sets. (a) group 10, (b) group 11, and (c) group 12. Other curves from several references are shown for comparison. Our curves of group 10 are the only ones available. For Ni^{+}-Xe, Ni was treated with Stuttgart basis set while Xe was treated with Sapporo basis set.

Table 3.2 Parameters of Interaction Potentials and Calculated Spectroscopic Constants

Potential	Reference	σ (Å)	R_e (Å)	D_e (cm^{-1})	D_0 (cm^{-1})	ω_e (cm^{-1})	$\omega_e x_e$ (cm^{-1})	B_0 (cm^{-1})	D_{J0} (cm^{-1})
Ni^+–Xe	Karlsruhe	2.24	2.63	6349					
	Stuttgart	2.11	2.49	8097	8003	190.3	1.18	0.067	3.32×10^{-8}
Pd^+–Xe	Sapporo	2.30	2.71	6838					
	Karlsruhe	2.31	2.76	6101					
	Stuttgart	2.26	2.69	7605	7531	148.3	0.70	0.040	1.15×10^{-8}
Pt^+–Xe	Sapporo	2.24	2.62	9969					
	Karlsruhe	2.25	2.67	7625					
	Stuttgart	2.19	2.59	11240	11156	160.6	0.81	0.032	4.77×10^{-9}
Cu^+–Xe	Sapporo	2.18	2.51	7335					
	Karlsruhe	2.16	2.59	6181					
	Stuttgart	2.18	2.53	7579	7493	172.4	0.97	0.061	3.19×10^{-8}
	Freitag et al.[1]		2.80	5100					
	Yousef et al.[6]	2.06	2.49	8301	8210	182.3	1.02	0.063	3.12×10^{-8}

Table 3.2 (continued)

Potential	Reference	σ (Å)	R_e (Å)	D_e (cm^{-1})	D_0 (cm^{-1})	ω_e (cm^{-1})	$\omega_e x_e$ (cm^{-1})	B_0 (cm^{-1})	D_{J0} (cm^{-1})
Ag^+–Xe	Sapporo	2.36	2.79	5211					
	Karlsruhe	2.39	2.83	4709					
	Stuttgart	2.33	2.76	5943	5879	129.4	0.80	0.037	1.28×10^{-8}
	Freitag et al.[1]		3.17	3070					
	Brock and Duncan[46]			>3900					
	Yousef et al.[6]	2.32	2.76	5864	5800	128.0	0.70	0.037	1.29×10^{-8}
Au^+–Xe	Sapporo	2.27	2.63	9399					
	Karlsruhe	2.23	2.64	8687					
	Stuttgart	2.24	2.60	10373	10297	152.3	0.67	0.031	5.38×10^{-9}
	Pykkö[2]		2.76	7340					
	Schröder et al.[22]		2.57	10600					
	Yousef et al.[6]	2.19	2.61	10063	9988	151.1	0.56	0.031	5.42×10^{-9}
	Breckenridge et al.[21]		2.60	10529		154.7	0.57		
	Zeng and Klobukowski[19]		2.64		8781	141.2	0.55		
	Belpassi et al.[20]		2.61		10710	150.0			

Table 3.2 (continued)

Potential	Reference	σ (Å)	R_e (Å)	D_e (cm^{-1})	D_0 (cm^{-1})	ω_e (cm^{-1})	$\omega_e x_e$ (cm^{-1})	B_0 (cm^{-1})	D_{J0} (cm^{-1})
Zn^+–Xe	Sapporo	2.43	2.82	4146					
	Karlsruhe	2.41	2.88	3850					
	Stuttgart	2.34	2.81	4805	4742	125.0	0.37	0.049	2.99×10^{-8}
	Lee et al.[5]	2.30	2.77	5088	5023	129.9	0.79	0.050	3.05×10^{-8}
Cd^+–Xe	Sapporo	2.60	3.06	3103					
	Karlsruhe	2.64	3.11	2832					
	Stuttgart	2.56	2.98	3707	3663	94.8	0.74	0.030	1.29×10^{-8}
	Qing et al.[4]		3.03	3705		93.2	0.60	0.030	
Hg^+–Xe	Sapporo	2.55	2.96	4589					
	Karlsruhe	2.53	2.99	4434					
	Stuttgart	2.48	2.93	5325	5274	102.6	0.046	0.025	5.82×10^{-9}
	Liao and Ng[47]		~2.8	6020±150					
	Qing et al.[4]		2.95	5237		100.7	0.44	0.024	

recent studies, pioneering theoretical works like those of Freitag et al. on Ag^+–Xe and Pykkö on Au^+–Xe reported low binding energies and long equilibrium distances.[1,2] This is because M^+–Xe interaction is dominated by the charge-induced interaction:

$$V = -\frac{\alpha}{2r^4} \qquad (1)$$

where α denotes the dipole polarizability of xenon. Advanced basis sets with extra polarization functions help describe the polarizability of xenon better and therefore lead to higher binding energies. Of the three basis sets used here, Stuttgart provides closest results to recent studies. This is attributable to the larger size of Stuttgart basis sets and the fact that these studies also employed the ECPs and basis sets of Stuttgart derivation. Our results show that the order in binding strength is group 12 < group 11 and row 4 < row 3 < row 5.

For Au^+–Xe system, there are gaps between the results of Zeng and Klobukowski who used MCPs and the results from Stuttgart ECPs of Schröder et al, Yousef et al., Breckenridge et al. and us. The D_e and R_e values by CCSD(T) calculations are (8781 cm^{-1}, 2.64 Å), (10600 cm^{-1}, 2.57 Å), (10063 cm^{-1}, 2.61 Å), (10529 cm^{-1}, 2.60 Å), and (10373 cm^{-1}, 2.60 Å), respectively. Zeng and Klobukowski also tried other newly developed CC methods. The CR-CCSD(TQ)_B, which they regarded as most accurate, yielded even smaller value for binding energy, (7895 cm^{-1}, 2.65 Å). The differences between MCP and ECP results are clearly due to the difference in nature between these two pseudopotentials. Results from ECPs are supported by the study of Belpassi et al., which has the largest dissociation energy D_0 for Au^+–Xe thus far, 10710 cm^{-1}.

Moving to group 10, there were a couple of problems arising with Sapporo and Karlsruhe calculations. Firstly, calculation using Sapporo basis set for Ni^+–Xe failed to converge. Secondly, D_e value for Pt^+–Xe is smaller than that of Au^+–Xe with Karlsruhe BS (8892 < 10088 cm^{-1}) while Sapporo and Stuttgart show the opposite trend (9969 > 9399 cm^{-1} for Sapporo and 11240 > 10373 cm^{-1} for Stuttgart). The results from Karlsruhe contradict our assumption that extra space in d orbitals of atoms in group 10 would assist xenon binding compared with those in group 11. Compared with Sapporo and Stuttgart, Karlsruhe basis set always provides the weakest bond strength for all 9 ion–xenon complexes. This is likely due to the lack of SO component in this BS. Because of these limitations of Sapporo and Karlsruhe basis sets and the good agreement between Stuttgart basis set results with previous studies in group 11 and 12, Stuttgart basis set was chosen for further LEVEL calculations and population analyses. The spectroscopic parameters obtained by LEVEL in Table 3.2 can be used for the model potential analysis which will be discussed later.

With Stuttgart basis set, the energetic order is group 12 < group 11 < group 10 and row 5 < row 4 < row 6. Au^+ has been considered to form the strongest bond with Xe, which is one of the reasons that Au^+–Xe has been received extensive attention. In this study, Pt^+ was found to bind to Xe stronger than Au^+. The dissociation energy and bond length for Pt^+ are 11156 cm^{-1} and 2.59 Å compared with 10297 cm^{-1} and 2.60 Å of Au^+. This finding promises some very interesting opportunities for further theoretical and experimental studies involving this interaction. In each group, although the cation from row 6 has the highest binding energy with xenon, it is the cation from row 4 which has

the shortest bond length. For example, D_e and R_e values for Ni, Pd, and Pt^+–Xe are (8097 cm^{-1}, 2.49 Å), (7605 cm^{-1}, 2.69 Å), and (11240 cm^{-1}, 2.59 Å), respectively.

3.3.2 Natural Bond Orbital Analysis

NBO analysis can provide insight into the nature of the donor–acceptor interaction of the M^+–Xe systems. The minimum point of each Stuttgart potential curve was chosen to perform the analysis with MP2 method. The natural atomic orbital (NAO) electronic occupancies and the natural charges of the atoms are shown in Table 3.3. The electronic configurations of each atom before and after binding as well as the difference between them are displayed. From the natural charges, there is always a total electron transfer from the TM ions to xenon. The largest of all is of Au^+–Xe and Pt^+–Xe (0.14 and 0.13 electron, respectively). In our study on Ag-Chabazite–Xe, results from silver clusters with different sizes from both the gas phase and the chabazite surface show a correlation between the interaction energies and the electron transfers.[3] In this study, unlike the order of binding energies, the charge transfer order cannot be established as group 12 < group 11 < group 10 and row 5 < row 4 < row 6. Correlation between the charge transfer and the binding strength might be limited to an individual element only, not a universal phenomenon between different elements. Nevertheless, one can at least conclude that the strongest ligand to xenon in each group is always the one with the largest charge transfer and it is the transition metals from row 6.

Specifically, the interaction between M^+ and Xe is characterized by the σ donation from the donor, xenon, to the acceptor, M^+. Electrons from the $5p_z$ orbital of Xe move to the *n*s orbital of M^+. For instance, the electronic occupancies of Pt^+'s 6s before and after

Table 3.3 Natural Atomic Orbital Electron Occupancies of Cations and Xenon before and after Binding

		Electronic configurations	Natural charges (M, Xe)
Ni^+–Xe	Ni^+_{before}	[core]$4s^0 3d^9 4p^0$	(0.94, 0.06)
	Ni^+_{after}	[core]$4s^{0.06} 3d^{8.99} 4p^{0.01}$	
	Ni^+_{Δ}	**[core]$4s^{0.06} 3d^{-0.01} 4p^{0.01}$**	
	Xe_{before}	[core]$5s^2 5p^6 5d^0$	
	Xe_{after}	[core]$5s^{1.99} 5p^{5.93} 5d^{0.02}$	
	Xe_{Δ}	**[core]$5s^{-0.01} 5p^{-0.07} 5d^{0.02}$**	
Pd^+–Xe	Pd^+_{before}	[core]$5s^0 4d^9 5p^0$	(0.90, 0.10)
	Pd^+_{after}	[core]$5s^{0.04} 4d^{9.03} 5p^{0.03}$	
	Pd^+_{Δ}	**[core]$5s^{0.05} 4d^{0.03} 5p^{0.03}$**	
	Xe_{Δ}	**[core]$5s^{-0.01} 5p^{-0.10} 5d^{0.01}$**	
Pt^+–Xe	Pt^+_{before}	[core]$6s^0 5d^9 6p^0$	(0.87, 0.13)
	Pt^+_{after}	[core]$6s^{0.17} 5d^{8.95} 6p^{0.01}$	
	Pt^+_{Δ}	**[core]$6s^{0.17} 5d^{-0.05} 6p^{0.01}$**	
	Xe_{Δ}	**[core]$5s^{-0.01} 5p^{-0.14} 5d^{0.02}$**	
Cu^+–Xe	Cu^+_{before}	[core]$4s^0 3d^{10} 4p^0$	(0.93, 0.07)
	Cu^+_{after}	[core]$4s^{0.06} 3d^{9.99} 4p^{0.01}$	
	Cu^+_{Δ}	**[core]$4s^{0.06} 3d^{-0.01} 4p^{0.01}$**	
	Xe_{Δ}	**[core]$5s^{-0.01} 5p^{-0.08} 5d^{0.01}$**	
Ag^+–Xe	Ag^+_{before}	[core]$5s^0 4d^{10} 5p^0$	(0.95, 0.05)
	Ag^+_{after}	[core]$5s^{0.05} 4d^{10.00} 5p^{0.01}$	
	Ag^+_{Δ}	**[core]$5s^{0.05} 4d^{0.00} 5p^{0.01}$**	
	Xe_{Δ}	**[core]$5s^{0.00} 5p^{-0.06} 5d^{0.01}$**	

Table 3.3 (continued)

		Electronic configurations	Natural charges (M, Xe)
Au^+–Xe	Au^+_{before}	$[core]6s^0 5d^{10} 6p^0$	(0.86, 0.14)
	Au^+_{after}	$[core]6s^{0.16} 5d^{9.96} 6p^{0.01}$	
	$\mathbf{Au^+_\Delta}$	$\mathbf{[core]6s^{0.16} 5d^{-0.04} 6p^{0.01}}$	
	$\mathbf{Xe_\Delta}$	$\mathbf{[core]5s^{-0.01} 5p^{-0.15} 5d^{0.01}}$	
Zn^+–Xe	Zn^+_{before}	$[core]4s^1 3d^{10} 4p^0$	(0.91, 0.09)
	Zn^+_{after}	$[core]4s^{1.05} 3d^{10.00} 4p^{0.03}$	
	$\mathbf{Zn^+_\Delta}$	$\mathbf{[core]4s^{0.05} 3d^{0.00} 4p^{0.03}}$	
	$\mathbf{Xe_\Delta}$	$\mathbf{[core]5s^{-0.01} 5p^{-0.10} 5d0^{.01}}$	
Cd^+–Xe	Cd^+_{before}	$[core]5s^1 4d^{10} 5p^0$	(0.94, 0.07)
	Cd^+_{after}	$[core]5s^{1.04} 4d^{10.00} 5p^{0.03}$	
	$\mathbf{Cd^+_\Delta}$	$\mathbf{[core]5s^{0.04} 4d^{0.00} 5p^{0.03}}$	
	$\mathbf{Xe_\Delta}$	$\mathbf{[core]5s^{0.00} 5p^{-0.08} 5d^{0.01}}$	
Hg^+–Xe	Hg^+_{before}	$[core]6s^1 5d^{10} 6p^0$	(0.90, 0.10)
	Hg^+_{after}	$[core]6s^{1.08} 5d^{9.99} 6p^{0.03}$	
	$\mathbf{Hg^+_\Delta}$	$\mathbf{[core]6s^{0.08} 5d^{-0.01} 6p^{0.03}}$	
	$\mathbf{Xe_\Delta}$	$\mathbf{[core]5s^{-0.01} 5p^{-0.11} 5d^{0.01}}$	

binding are 0 and 0.17, while those values of Xe's 5p are 6 and 5.86. The unbalance between the gain and loss of *n*s and 5p is because of the contribution of other orbitals of M^+ into the binding. This phenomenon is more pronounced in group 10 with the $(n\text{-}1)d^9$ subshells and in group 12 with the np^0 subshells. In contradiction with the our proposed role of the open $(n\text{-}1)d^9$ subshells in binding xenon, they do not always receive electron. The changes of number of electrons in $(n\text{-}1)d^9$ are -0.01, 0.03, and -0.05 for Ni^+, Pd^+, and Pt^+–Xe, respectively. For group 12, np^0 of each cation gains 0.03 electron after binding. $(n\text{-}1)d^{10}$ and np^0 of group 11 also have a role in the binding, however, less obvious. Using the σ donation as an indicator for the covalency, we can conclude that chemical bonding only occurs in complexes with significant electron sharing (> 0.1 electron). They are Pd^+, Pt^+, Au^+, and Hg^+–Xe.

Several studies confirmed that the chemical bonding occurs in Au^+–Xe system.[19-21] The resolution came from three approaches – the NBO, the electron density, and the model potential analyses. The model analysis is used to decide whether a bonding is physical, namely if the bonding can be described by a charge-induced interaction like in equation (1) (plus other induction and dispersion terms dependent on $1/r^6$, $1/r^7$, $1/r^8$, etc.).[11] In the model potential analysis, if an M^+–Xe interaction is entirely physical, the calculated charge Z of the cation should be close to 1.00. Z for Au^+–Xe ranges from 1.42 to 1.45, which is unphysically but logically high to account for the covalent contribution.[11,21] Or in other words, a chemical bond is formed between Au^+ and Xe.

Bellert and Brickenridge presented a list of results of model potential analysis for many ion–Rgs complexes.[13] In that list, Au^+–Xe is the only chemical compound and possesses the highest dissociation energy. Cu^+ and Ag^+–Xe are physical compounds. No

other systems of interest of this study were presented. Our calculations shows that (i) Pt^+ has higher binding energy than Au^+, and (ii) the σ donations for both cases are similar to each other and are the largest of all ion–Xe complexes. Therefore, we can predict that Pt^+–Xe interaction is chemical under a model potential analysis. Other pairs including Pd^+ and Hg^+–Xe fall into the physical category because their bond strengths are similar to Cu^+ and Ag^+–Xe. However, one needs to notice that the demarcation line between chemical and physical is blurred because of the vague and subjective definition of covalency (Charge transfer > 0.1 electron in our NBO study and Z = 1.00 ± 0.1 in Bellert and Breckenridge's model potential). The inconsistency in judging the covalency under different approaches clearly proves the obscurity of this subject.

3.4 Summary

The interaction potentials for Xe and nine transition metal cations of group 10, 11, and 12, which are Ni^+, Pd^+, Pt^+, Cu^+, Ag^+, Au^+, Zn^+, Cd^+, and Hg^+, are presented. This is the first time these potentials were studied together at levels of theory that are directly comparable, and also the first time the transition metals of group 10 were investigated. Basis sets from three different laboratories were evaluated. The relativistic effects, which are crucial for heavy metals, were included through the use of pseudopotentials or an approximate DK3 Hamiltonian. Our results agree well with other recent studies for group 11 and 12. We found that the strength of xenon binding follows the trend with group 12 < group 11 < group 10 and row 5 < row 4 < row 6. Pt^+ interacts with Xe stronger than Au^+ and is the strongest ligand to Xe ever reported. Finally, natural bond orbital analysis was done for all nine complexes. A σ donation from 5p orbital of Xe to *n*s orbital of the ions

was observed. Au^+ and Pt^+ have the largest σ donation. We suggested that, in the Au^+–Xe and Pt^+–Xe complexes, chemical bonds were formed.

3.5 References

(1) Freitag, A.; van Wüllen, C.; Staemmler, V. *Chem. Phys.* **1995**, *192*, 267.

(2) Pyykkö, P. *J. Am. Chem. Soc.* **1995**, *117*, 2067.

(3) Nguyen, H. G.; Konya, G.; Eyring, E. M.; Hunter, D. B.; Truong, T. N. *J. Phys. Chem. C* **2009**, *113*, 12818.

(4) Qing, E.; Viehland, L. A.; Lee, E. P. F.; Wright, T. G. *J. Chem. Phys.* **2006**, *124*, 044316.

(5) Lee, E. P. F.; Gray, B. R.; Joyner, N. A.; Johnson, S. H.; Viehland, L. A.; Breckenridge, W. H.; Wright, T. G. *Chem. Phys. Lett.* **2007**, *450*, 19.

(6) Yousef, A.; Shrestha, S.; Viehland, L. A.; Lee, E. P. F.; Gray, B. R.; Ayles, V. L.; Wright, T. G.; Breckenridge, W. H. *J. Chem. Phys.* **2007**, *127*, 154309.

(7) Konya, G.; Eyring, E. M.; Hunter, D., unpublished work., University of Utah, USA.

(8) Barrer, R. M.; Papadopoulos, R. *Proc. R. Soc. Lond. A* **1972**, *326*, 315.

(9) Munakata, K.; Kanjo, S.; Yamatsuki, S.; Koga, A.; Ianovski, D. *J. Nucl. Sci. Technol.* **2003**, *40*, 695.

(10) Kuznicki, S. M.; Anson, A.; Koenig, A.; Kuznicki, T. M.; Haastrup, T.; Eyring, E. M.; Hunter, D. *J. Phys. Chem. C* **2007**, *111*, 1560.

(11) Bellert, D.; Breckenridge, W. H. *Chem. Rev.* **2002**, *102*, 1595.

(12) Vaval, N.; Bililign, S.; Gdanitz, R. J. *Chem. Phys.* **2003**, *290*, 171.

(13) Hickling, H. L.; Viehland, L. A.; Shepherd, D. T.; Soldán, P.; Lee, E. P. F.; Wright, T. G. *Phys. Chem. Chem. Phys.* **2004**, *6*, 4233

(14) Ono, Y.; Taketsugu, T.; Noro, T. *J. Chem. Phys.* **2005**, *123*, 204321.

(15) Shen, Y.; BelBruno, J. J. *J. Phys. Chem. A* **2005**, *109*, 10077.

(16) Taketsugu, Y.; Taketsugu, T.; Noro, T. *J. Chem. Phys.* **2006**, *125*, 154308.

(17) Plowright, R. J.; Ayles, V. L.; Watkins, M. J.; Gardner, A. M.; Wright, R. R.; Wright, T. G.; Breckenridge, W. H. *J. Chem. Phys.* **2007**, *127*, 204308.

(18) Lovallo, C. C.; Klobukowski, M. *Chem. Phys. Lett.* **2003**, *368*, 589.

(19) Zeng, T.; Klobukowski, M. *J. Phys. Chem. A* **2008**, *112*, 5236.

(20) Belpassi, L.; Infante, I.; Tarantelli, F.; Visscher, L. *J. Am. Chem. Soc.* **2007**, *130*, 1048.

(21) Breckenridge, W. H.; Ayles, V. L.; Wright, T. G. *J. Phys. Chem. A* **2008**, *112*, 4209.

(22) Schröder, D.; Schwarz, H.; Hrusak, J.; Pyykko, P. *Inorg. Chem.* **1998**, *37*, 624.

(23) Partridge, H.; Bauschlicher, C. W.; Langhoff, S. R. *J. Phys. Chem.* **1992**, *96*, 5350.

(24) Velegrakis, M.; Froudakis, G. E.; Farantos, S. C. *J. Chem. Phys.* **1998**, *109*, 4687.

(25) Burda, J. V.; Runeberg, N.; Pyykkö, P. *Chem. Phys. Lett.* **1998**, *288*, 635.

(26) Rao, K. S.; Stoicheff, B. P.; Turner, R. *Can. J. Phys.* **1960**, *38*, 1516.

(27) Reiher, M.; Wolf, A. *J. Chem. Phys.* **2004**, *121*, 2037.

(28) Glendening, E. D.; Badenhoop, J. K.; Reed, A. E.; Carpenter, J. E.; Bohmann, J. A.; Morales, C. M.; Weinhold, F. 2001.

(29) Koga, T.; Tatewaki, H.; Shimazaki, T. *Chem. Phys. Lett.* **2000**, *328*, 473.

(30) Noro, T.; Sekiya, M.; Koga, T.; Matsuyama, H. *Theo. Chem. Acc.* **2000**, *104*, 146.

(31) Sekiya, M.; Noro, T.; Osanai, Y.; Koga, T. *Theo. Chem. Acc.* **2001**, *106*, 297.

(32) Osanai, Y.; Sekiya, M.; Noro, T.; Koga, T. *Mol. Phys.* **2003**, *101*, 65.

(33) Osanai, Y.; Noro, T.; Miyoshi, E.; Sekiya, M.; Koga, T. *J. Chem. Phys.* **2004**, *120*, 6408.

(34) Weigend, F.; Ahlrichs, R. *Phys. Chem. Chem. Phys.* **2005**, *7*, 3297

(35) Peterson, K. A.; Figgen, D.; Goll, E.; Stoll, H.; Dolg, M. *J. Chem. Phys.* **2003**, *119*, 11113.

(36) Balabanov, N. B.; Peterson, K. A. *J. Chem. Phys.* **2005**, *123*, 064107.

(37) Figgen, D.; Rauhut, G.; Dolg, M.; Stoll, H. *Chem. Phys.* **2005**, *311*, 227.

(38) Figgen, D.; Peterson, K. A.; Stoll, H. *J. Chem. Phys.* **2008**, *128*, 034110.

(39) Peterson, K. A.; Figgen, D.; Dolg, M.; Stoll, H. *J. Chem. Phys.* **2007**, *126*, 124101.

(40) Nakajima, T.; Hirao, K. *J. Chem. Phys.* **2000**, *113*, 7786.

(41) H.-J. Werner, P. J. K., R. Lindh, F.R. Manby, M. Schütz, et al 2008.

(42) Runeberg, N.; Pyykkö, P. *Int. J. Quantum Chem.* **1998**, *66*, 131.

(43) Chalasinski, G.; Szczesniak, M. M. *Chem. Rev.* **2000**, *100*, 4227.

(44) Simon, S.; Duran, M.; Dannenberg, J. J. *J. Chem. Phys.* **1996**, *105*, 11024.

(45) LeRoy, R. J.; University of Waterloo Chemical Physics Research Program Report CP-555R: 2000.

(46) Brock, L. R.; Duncan, M. A. *J. Chem. Phys.* **1995**, *103*, 9200.

(47) Liao, C. L.; Ng, C. Y. *J. Chem. Phys.* **1986**, *84*, 1142.

CHAPTER 4

DIFFUSION OF XENON THROUGH THE 8T RING OF CHABAZITE

4.1 Introduction

Diffusion of adsorbed molecules in zeolite crystals is critical for applications of zeolites as adsorbents and shape-selective catalysts.[1-5] For this dissertation, study of the diffusion of xenon in chabazite helps to identify the active sites that bind xenon. Although it is established from Chapter 2 and 3 that silver particles in chabazite bind zeolite, the remaining question is whether they are on the surface of the material or inside the cage of chabazite. The answer to this question will assist further experimental efforts to tailor suitable materials for xenon binding.

In recent years, the combination of transition state theory (TST) and the calculation of the dynamic corrections has been a reliable approach for the simulation of zeolitic systems. Monte Carlo (MC) and molecular dynamics (MD) are usually used for this purpose with good results. Although these methods are very powerful, they are limited by the accuracy with which the force field can be calculated and by the bulk of MD simulations. For xenon inside zeolite, there is only on theoretical study by Mosell et al.[6]
In this chapter, quantum mechanics calculations to study the intracrystalline diffusion of xenon in chabazite were performed. The rate constants by which xenon passing through the largest ring of chabazite, the 8T ring, are calculated using the canonical transition state theory (CVT).[7-9] The symmetry of the transition state of xenon being in the middle

of the 8T ring was exploited to obtain accurate structural and frequency information. The rate constants are then used in the hopping model to calculate the diffusion coefficients.

4.2 Methodology

In this study, the reactant and product for kinetic calculations are the optimal structure of a xenon atom inside the chabazite cage. The transition state structure is when xenon positions itself at the center of an 8T ring to move to an adjacent cage (Figure 4.1). The quantum cluster of the 8T ring and xenon used in this study is $Si_8O_{24}H_{16}$-Xe. The diffusion of xenon inside chabazite is described by the hopping model. A xenon atom inside one chabazite cage can jump to neighboring cages through the 8T rings. For each cage, there are total six neighbor cages as presented in Figure 4.2. Cage-to-cage jumps are the rate-determining event. Length of the jump (Δr) is the distance between the two adjacent cages. The diffusion coefficient is given by

$$D = \frac{1}{2} k_{TST} \Delta r^2 \sum_n cos^2 \varphi_n \qquad (1)$$

where φ_n is the angle between the direction of the jump and the direction of the diffusion. n is the number of the neighboring cages ($n = 6$ for chabazite). If z direction is chosen, $\varphi_n = 42.8°, \Delta r = 10.05$Å.

All electronic structure calculations were carried out using the program package Gaussian 03. The Stuttgart correlation-consistent polarized valence triple-zeta basis set (aug-cc-pVTZ-PP) was employed with DFT method to determine the optimized structures and vibrational frequencies for the stationary points. To correctly describe the

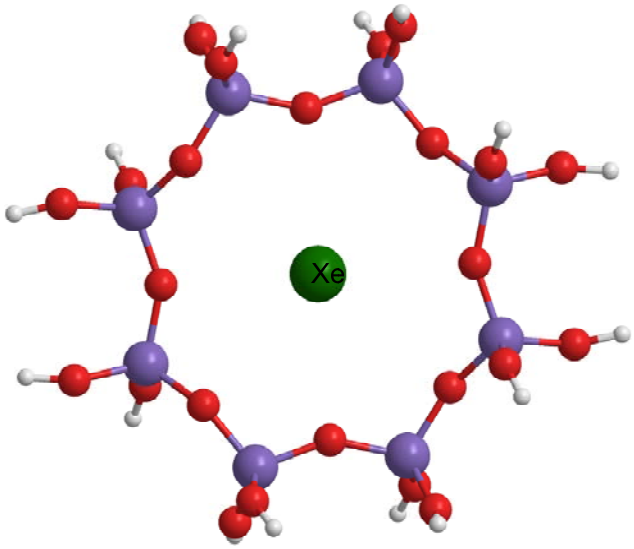

Figure 4.1 Xenon in the middle of the 8T ring of chabazite ($Si_8O_{24}H_{16}$-Xe).

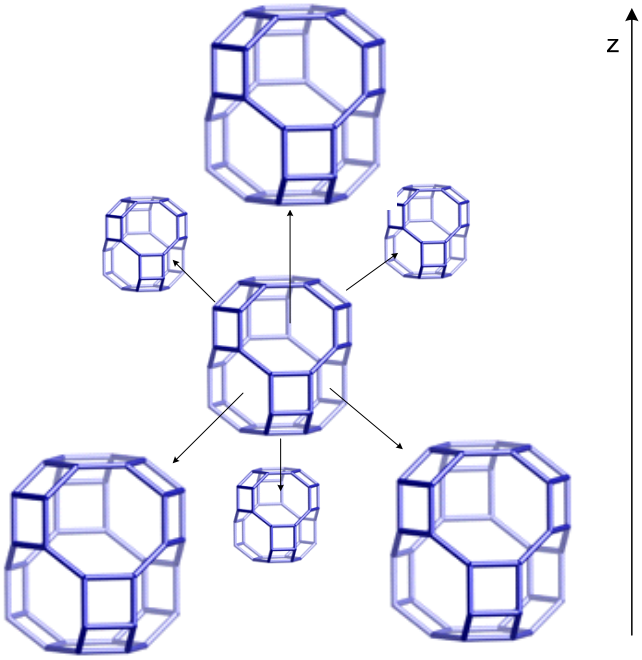

Figure 4.2 A chabazite cage with six neighbor cages.

dispersion interaction which occurs due to the zeolite channel wall, the Grimme's functional B97D was used.[10] This functional is a generalized gradient approximation (GGA) type and includes long-range pairwise dispersion corrections.

The minimum energy path (MEP), illustrated in Figure 4.3, was also obtained at the same B97D/aug-cc-pVTZ-PP level by tracing the steepest descent path from the transition states to the products and reactants using the Gonzalez-Schlegel method with a step size of 0.5 $(amu)^{1/2}$bohr for a total of 20 steps. Force constant calculations along the MEP were carried out to obtain the necessary potential energy surface information for CVT calculations. To incorporate the effect of the crystal framework on the energy barrier, the SCREEP and the FQEC models which are discussed in the first chapter were employed.[11,12] TST and CVT calculations were carried out using TheRate program.

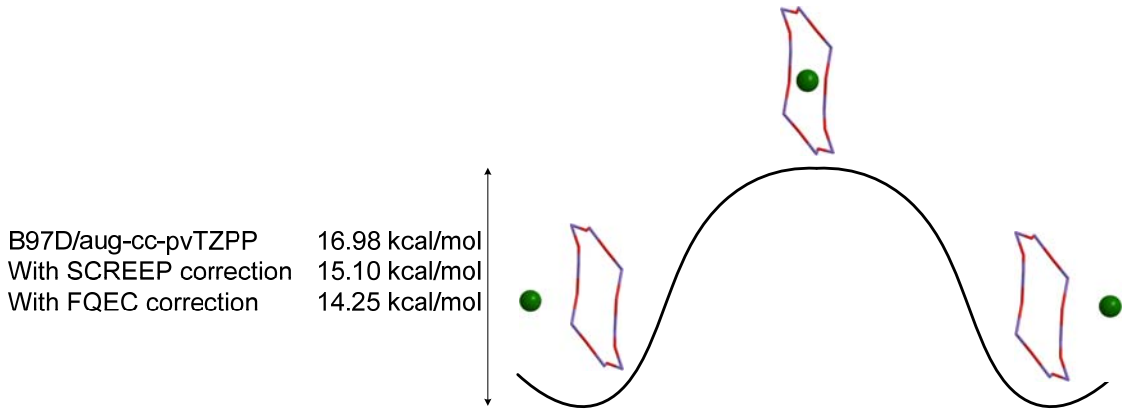

Figure 4.3 Schematic energy profile of the passing of xenon through 8T ring, at different levels of theory as indicated.

4.3 Results and Discussion

Optimized struc ture of the 8T-Xe system is shown in Figure 4.1. With one xenon atom in the middle of the 8T ring, the distance between two opposite Si atoms increases from 8.05 Å to 8.06 Å. The corresponding distance for oxygen changes from 6.39 to 6.41 Å. The Si-O-Si angle changes from 145.3° to 148.0°. The barrier height is 16.98 kcal/mol for the cluster model at B97D/aug-cc-pvTZPP level. Corrections by SCREEP and FQEC bring this barrier height down to 15.10 and 14.25 kcal/mol. The reason for the decrease of the barrier height is the steric effect of the framework which raises the energy of the optimized structure of the xenon inside the chabazite cage.

The calculated rate constants using the TST and CVT method in the temperature range of 300-1000 K are given in Table 4.1. The ratio between the rate constants k^{CVT}/k^{TST} illustrate the magnitude of the re-crossing effect. It can be seen that this ratio increases as the temperature increases; thus the re-crossing effect is less important at high temperature. At room temperature, the re-crossing effect without SCREEP and FQEC corrections accounts for 51% of the total rate. However at 100K, it only lowers the rate constants by 15%.

Due to the relatively flat shape the V_{EMP} curve in the transition state region and barrier being quite low, the tunneling effect can be expected to have very small contribution to the rate constant and was ignored in our calculation. This decision is confirmed by the linearity of the rate plot in Figure 4.4. The Arrhenius expressions for the rate constants calculated with the CVT for cluster model, SCREEP model, and FQEC are

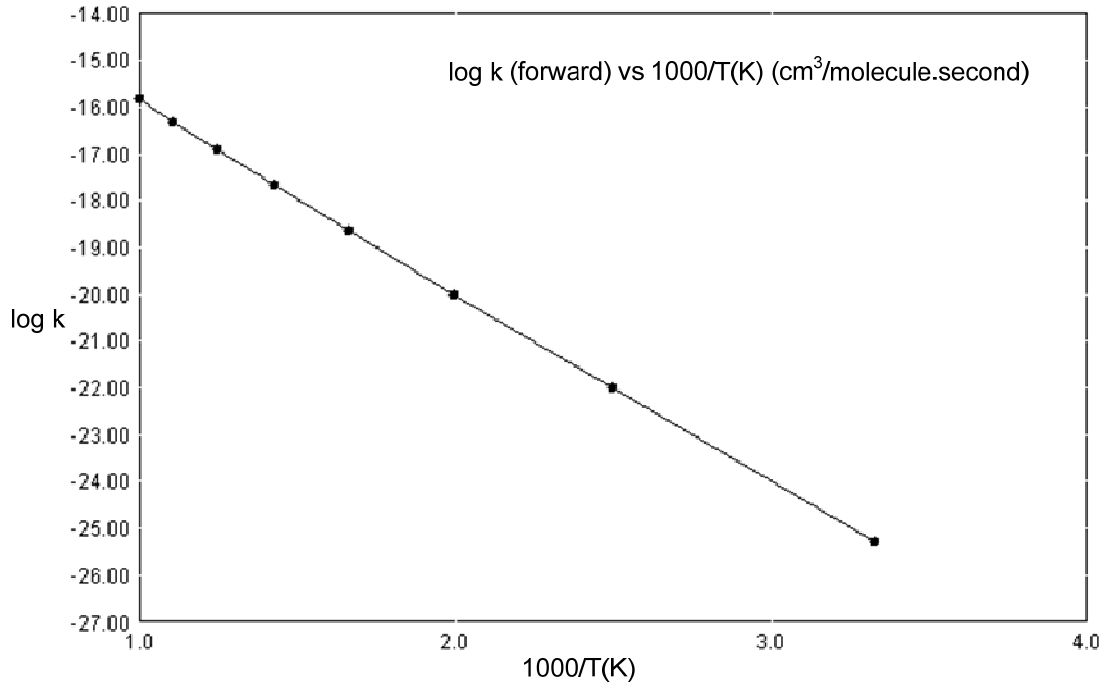

Figure 4.4 Arrhenius plot of the CVT rate constants with FQEC correction.

Table 4.1 TST and CVT Rate Constants ($cm^3molecule^{-1}s^{-1}$) and Diffusion Coefficients Using Cluster Model

T(K)	k^{TST}	k^{CVT}/k^{TST}	D ($cm^2s^{-1)}$
300	5.186E-26	0.49	1.04E-13
400	9.946E-23	0.55	1.99E-10
500	1.001E-20	0.64	2.00E-08
600	2.278E-19	0.68	4.56E-07
700	2.201E-18	0.73	4.40E-06
800	1.239E-17	0.75	2.48E-05
900	4.850E-17	0.77	9.70E-05
1000	1.469E-16	0.78	2.94E-04

$$k(t) = 1.58 \times 10^{-15} \times T^{0.929} \times exp\left(\frac{8848}{T}\right), \text{cm}^3\text{molecule}^{-1}\text{s}^{-1}$$

$$k(t) = 1.58 \times 10^{-15} \times T^{0.929} \times exp\left(\frac{7900}{T}\right), \text{cm}^3\text{molecule}^{-1}\text{s}^{-1}$$

$$k(t) = 1.58 \times 10^{-15} \times T^{0.929} \times exp\left(\frac{7474}{T}\right), \text{cm}^3\text{molecule}^{-1}\text{s}^{-1}$$

Using equation (1), the diffusion coefficients determined by hopping model for xenon in chabazite through z direction using SCREEP and FQEC corrections are given in Table 4.2 and 4.3. Compared with the latest values of the rate constants available in the literature, our results show much slower diffusion rates. Mosell et al. reported 1.0×10^{-5} cm^2/s at room temperature for Y zeolite. This is because the largest ring in Y zeolite is the 10T ring while it is the 8T ring for chabazite. The barrier height in Y zeolite is 7 kcal/mol compared with 13 kcal/mol of this study. From our results, xenon diffuses extremely slowly inside chabazite. This conclusion agrees with the circumstantial data that xenon cannot penetrate the pores of Ag-exchanged chabazite.

4.4 Summary

In this chapter, the kinetics of xenon passing through 8T ring of chabazite is studied using the variational canonical transition state theory. The potential energy information was calculated from a sufficiently accurate level of theory. In particular, structural and frequency information along the reaction coordinate were calculated at the B97D/aug-cc-pVTZ-PP level. Energy corrections were included to describe the effect of the chabazite crystal by using the SCREEP and FQEC models. We found that the variational/re-crossing effect is important to this reaction, especially at low temperature range where the

Table 4.2 TST and CVT Rate Constants ($cm^3molecule^{-1}s^{-1}$) and Diffusion Coefficients with SCREEP Corrections

T(K)	k^{TST}	k^{CVT}/k^{TST}	D ($cm^2s^{-1)}$
300	1.220E-24	0.47	2.44E-12
400	1.062E-21	0.54	2.12E-09
500	6.656E-20	0.62	1.33E-07
600	1.105E-18	0.68	2.21E-06
700	8.517E-18	0.74	1.70E-05
800	4.048E-17	0.75	8.10E-05
900	1.389E-16	0.77	2.78E-04
1000	3.789E-16	0.77	7.58E-04

Table 4.3 TST and CVT Rate Constants ($cm^3molecule^{-1}s^{-1}$) and Diffusion Coefficients with FQEC corrections

T(K)	k^{TST}	k^{CVT}/k^{TST}	D ($cm^2s^{-1)}$
300	5.063E-24	0.47	1.01E-11
400	3.089E-21	0.53	6.18E-09
500	1.564E-19	0.63	3.13E-07
600	2.251E-18	0.68	4.50E-06
700	1.567E-17	0.74	3.13E-05
800	6.903E-17	0.75	1.38E-04
900	2.233E-16	0.77	4.47E-04
1000	5.808E-16	0.77	1.16E-03

rate constants are lowered by a factor up to 2. The diffusion coefficients were calculated using the hopping model. The diffusion coefficients with the corrections agree well with those scattered available data in literature. Therefore, the rate constant expression can be used confidently for the whole temperature 300-1000K.

4.5 References

(1) *Handbook of Zeolite Science and Technology*; Auerbach, S. M.; Carrado, K. A.; Dutta, P. K., Eds.; Marcel Dekker, Inc., 2003.

(2) Cejka, J.; Bekkum, H. v.; Corma, A.; Schüth, F. *Introduction to Zeolite Science and Practice*; Elsevier, 2007.

(3) Garlarneau, A.; Renzo, F. D.; Fajula, F.; Vedrine, J. *Zeolites and Mesoporous Materials at The Dawn of The 21st Century*; Elsevier, 2001.

(4) Kärger, J.; Ruthven, D. M. *Diffusion in Zeolites and other Microporous Solids*; Wiley: New York, 1992.

(5) Manning, J. R. *Diffusiton Kinetics for Atoms in Crystals*; D. Van Nostrand Co.: Princeton, 1968.

(6) Mosell, T.; Schrimpf, G.; Brickmann, J. *J. Chem. Phys* **1996**, *100*, 4582.

(7) Truhlar, D. G.; Garrett, B. C. *Accounts Chem. Res.* **1980**, *13*, 440.

(8) Truong, T. N.; Truhlar, D. G. *J. Chem. Phys* **1994**, *93*, 1761.

(9) Truhlar, D. G.; Isaccson, A. D.; Garrett, B. C. In *Theory of Chemical Reaction Dynamics*; Baer, M., Ed.; Springer: Berling, 1985.

(10) Grimme, S. *Journal of Computational Chemistry* **2006**, *27*, 1787.

(11) Stefanovich, E. V.; Truong, T. N. *Journal of Physical Chemistry B* **1998**, *102*, 3018.

(12) Treesukol, P.; Lewis, J. P.; Limtrakul, J.; Truong, T. N. *Chemical Physics Letters* **2001**, *350*, 128.